

MULTI-FIDELITY MACHINE LEARNING FOR PEROVSKITE BAND GAP PREDICTIONS

by

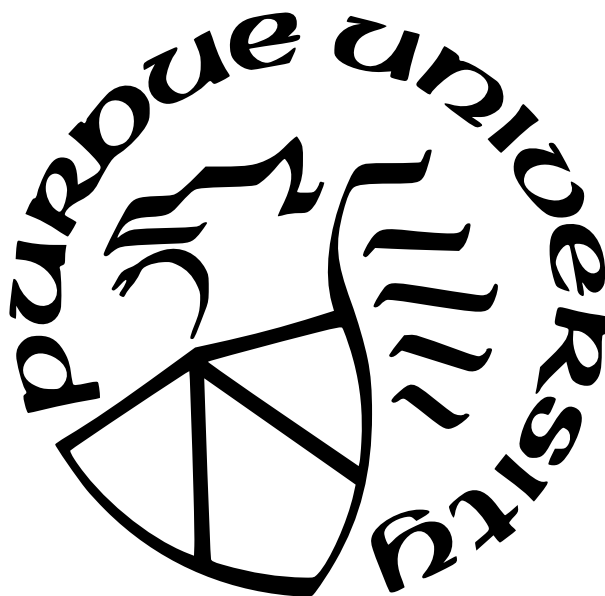
Panayotis T. Manganaris

A Thesis

Submitted to the Faculty of Purdue University

In Partial Fulfillment of the Requirements for the degree of

Master of Science



School of Materials Engineering

West Lafayette, Indiana

May 2023

**THE PURDUE UNIVERSITY GRADUATE SCHOOL
STATEMENT OF COMMITTEE APPROVAL**

Dr. Arun Mannodi-Kanakkithodi, Chair

School of Materials Engineering

Dr. Alejandro Strachan

School of Materials Engineering

Dr. Kendra Erk

School of Materials Engineering

Approved by:

Pending FORM 9 Approval

To my family, especially my brother Tassos.

ACKNOWLEDGMENTS

I am grateful to Professor Arun Mannodi-Kanakkithodi for his mentorship, support, and knowledge, Professor Erk for her guidance and counsel, and Professor Strachan for his instruction. I also thank my colleague Jiaqi Yang for his collaboration, and Habibur Rahman for his friendship and curiosity. My work was funded in part by my advisor’s startup grant F.10023800.05.002 and the Ross Fellowship awarded to me by Purdue University. The Rosen Center of Advanced Computing provided the computational resources needed to conduct simulations, store data, and train models.

TABLE OF CONTENTS

| | |
|--|----|
| LIST OF TABLES | 6 |
| LIST OF FIGURES | 7 |
| LIST OF LISTINGS | 8 |
| LIST OF SYMBOLS | 9 |
| ABBREVIATIONS | 10 |
| NOMENCLATURE | 11 |
| GLOSSARY | 12 |
| ABSTRACT | 14 |
| 1 INTRODUCTION | 15 |
| 1.1 Design Goals and Challenges in Perovskite PV Absorbers | 17 |
| 1.2 Multiple Fidelity Dataset | 21 |
| 2 DENSITY FUNCTIONAL THEORY SIMULATION | 22 |
| 2.1 DFT Computed Band Gaps | 24 |
| 2.2 Spectroscopic Limited Maximum Efficiency (SLME) | 24 |
| 2.3 Improving Property Predictions using HSE06 and Spin-Orbit Coupling | 25 |
| 2.4 Sampling the Halide Perovskite Chemical Space | 28 |
| 3 Multi-fidelity Machine Learning for Perovskite Band Gap Predictions | 32 |
| 3.1 Multi-Fidelity Learning | 32 |
| 3.2 Multiple Fidelity Dataset | 33 |
| 3.2.1 Perovskite Band Gaps | 33 |
| 3.2.2 Sampling | 35 |
| 3.2.3 Model Optimization | 35 |
| 3.3 Methods | 37 |

| | | |
|-------|--|----|
| 3.3.1 | DFT Details | 37 |
| 3.3.2 | Featurization of Chemistries | 38 |
| 3.3.3 | Machine Learning Algorithms and Parameter Optimization | 39 |
| 3.3.4 | Feature Engineering | 41 |
| 3.4 | Results | 42 |
| 3.4.1 | Best Models on Raw Domain | 42 |
| 3.4.2 | SISSO Model and SIS Engineered Features | 43 |
| 3.4.3 | Best Models on Engineered Domain | 45 |
| 3.5 | Discussion | 46 |
| 3.5.1 | SHAP Analysis of Domain | 46 |
| 3.5.2 | Predictions and Screening | 49 |
| 4 | PUBLICATIONS | 52 |
| 5 | PRESENTATIONS | 53 |
| 6 | SOFTWARE AND DATA CONTRIBUTIONS | 54 |
| 6.1 | Data Publication | 54 |
| 6.2 | Software Tools | 54 |
| 6.3 | Tutorials | 55 |

LIST OF TABLES

| | | |
|-----|---|----|
| 1.1 | ABX ₃ candidate species per site | 19 |
| 2.1 | Sample counts by density functional represented in dataset | 23 |
| 2.2 | RMSE values of band gaps computed from different functionals compared with experimental (Exp) values | 28 |
| 3.1 | Sample counts by density functional represented in dataset | 33 |
| 3.2 | ABX ₃ Chemical Domain | 35 |
| 3.3 | operations for formation of combinatorial super-space | 42 |
| 3.4 | RMSE of models on raw domain calculated per LoT subset | 44 |

LIST OF FIGURES

| | | |
|------|--|----|
| 1.1 | Rapid rise in cumulative maximum of HaP PCEs | 16 |
| 1.2 | $2 \times 2 \times 2$ α -phase supercell with Methylammonium at the A-site | 18 |
| 1.3 | The cardinal mixing sample space contains equal fractions of each element . . . | 20 |
| 1.4 | The cardinal mixing sample space contains mostly B-site mixed compounds . . . | 20 |
| 2.1 | PBE SLME of sample compares to experimental PCE and cleanly demarcates competitive range of band gaps | 26 |
| 2.2 | Variability in sampled band gaps at each fidelity | 27 |
| 2.3 | Effect of level of theory on band gap measurement | 28 |
| 2.4 | Share by count of total data apportioned from each experimental subcategory . | 29 |
| 2.5 | Samples overlaid on cardinal mixing chemical domain projected from fourteen to two dimensions via t-SNE | 30 |
| 3.1 | Variability in band gaps at each fidelity | 34 |
| 3.2 | Samples overlaid on cardinal mixing chemical domain projected from fourteen to two dimensions via t-SNE | 36 |
| 3.3 | model predictions vs true values at multiple fidelities | 42 |
| 3.4 | SIS-based model predictions vs true values at multiple fidelities | 45 |
| 3.5 | Random Forest Regression Band Gap SHAP Values | 47 |
| 3.6 | Gaussian Process Regression Band Gap SHAP Values | 47 |
| 3.7 | raw features with ($ p > 0.5$) against band gap | 48 |
| 3.8 | SHAP score distributions reveal effects of individual constituents | 49 |
| 3.9 | Band gap predictions overlaid on cardinal mixing chemical domain projected from fourteen to two dimensions via t-SNE | 50 |
| 3.10 | Frequency of mixing fractions of species at the A, B, and X sites across the ~3000 screen compounds | 51 |
| 1 | Normalized Distribution of A-site Constituents | 57 |
| 2 | Normalized Distribution of B-site Constituents | 58 |
| 3 | Normalized Distribution of X-site Constituents | 58 |
| 4 | Distributions of Mean A-Site Properties | 59 |
| 5 | Distributions of Mean B-Site Properties | 60 |
| 6 | Distributions of Mean X-Site Properties | 61 |

| | | |
|----|--|----|
| 7 | Gaussian Process Regression Band Gap SHAP Values | 61 |
| 8 | Random Forest Regression Band Gap on SIS domain SHAP Values | 62 |
| 9 | Gaussian Process Regression Band Gap on SIS domain SHAP Values | 62 |
| 10 | Projection of sample space via t-SNE overlaid with labels indicating site of mixing | 63 |
| 11 | Projection of sample space via t-SNE overlaid with labels indicating presense of data points in screened subset | 64 |

LIST OF LISTINGS

| | | |
|-----|--|----|
| 3.1 | An example of the cmcl "ft" feature accessor | 38 |
| 3.2 | Data frame of composition vectors generated by cmcl | 38 |
| 6.1 | How to load the Mannodi Group halide perovskites data set from the Materials Data Facility repository | 54 |

LIST OF SYMBOLS

| | |
|-----------|--------------------------------------|
| γ | photon |
| J | Current Density |
| I_{sun} | Light Spectrum Intensity of Sunlight |
| P | power |

ABBREVIATIONS

| | |
|-------|--|
| HaP | halide perovskite |
| VASP | Vienna Ab initio Simulation Package |
| SLME | spectroscopic limited maximum efficiency |
| PCE | power conversion efficiency |
| DFT | density functional theory |
| GGA | generalized gradient approximation |
| PBE | Perdew-Burke-Ernzerhof Functional |
| HSE06 | Heyd-Scuseria-Ernzerhof Functional |
| PCA | principal component analysis |
| t-SNE | t-distributed stochastic neighbor embedding |
| UMAP | uniform manifold approximation and projection |
| GPR | Gaussian Process Regression |
| RFR | Random Forest Regression |
| SISSO | Sure Independence Screening and Sparsifying Operator |
| SQS | special quasi-random structures |
| PAW | projector augmented wave |
| SHAP | Shapley Additive Explanation |

NOMENCLATURE

MA Methylammonium (Cationic Methylamine) CH_3NH_3^+

FA Formamidinium (Cationic Formamidine) $\text{CH}(\text{NH}_2)_2^+$

GLOSSARY

| | |
|--------------------|---|
| Law of Mixing | The rule stating properties of materials of mixed compositions may be predicted by linear interpolation of the properties of similar materials with pure compositions |
| cardinal mixing | Describes perovskite alloys where no more than one of the A, B, or X sites is occupied by multiple possible constituents |
| partition | Portion of sample data reserved for a purpose in model development |
| cross-validation | Method for gathering statistics on the abilities of a model to fit to the parent partition |
| K-fold split | Data partition divided into K arbitrary groups for use in cross-validation schemes |
| groupwise K-fold | Data partition divided into K-folds where each fold corresponds to a category label |
| level of theory | Refers to the rank of a DFT functional in the hierarchy of phenomenological comprehensiveness. A proxy for accuracy. |
| Materials Project | US Government-led multidisciplinary collaboration founded in 2011 as the Materials Genome Initiative. |
| machine learning | a science concerned with algorithms which improve their performance with exposure to new data |
| features | attributes of an observed event or object which might empirically explain the event or object |
| hyper-parameter | a setting that controls how a learning algorithm works |
| classical learning | a paradigm of machine learning that is dependent on expert knowledge to extract quality features from samples in a dataset |
| surrogate model | a representation which attempts to capture as much of the relationship between a domain and a target property as possible |
| deep learning | a paradigm of machine learning differing from classical learning in that the features of the input data are themselves learned by the algorithm |

| | |
|---------------------|--|
| FAIR | Findable Accessible Interoperable and Reusable Data |
| multi-task learning | A type of machine learning where an algorithm learns multiple functions simultaneously, while exploiting commonalities and differences between the functions |
| Spin Orbit Coupling | An additional term intended to account for the increased relevance of quantum angular momentum to electromagnetic response in heavy atoms |

ABSTRACT

A wide range of optoelectronic applications demand semiconductors optimized for purpose. My research focused on data-driven identification of ABX_3 Halide perovskite compositions for optimum photovoltaic absorption in solar cells. I trained machine learning models on previously reported datasets of halide perovskite band gaps based on first principles computations performed at different fidelities. Using these, I identified mixtures of candidate constituents at the A, B or X sites of the perovskite supercell which leveraged how mixed perovskite band gaps deviate from the linear interpolations predicted by Vegard’s law of mixing to obtain a selection of stable perovskites with band gaps in the ideal range of 1 to 2 eV for visible light spectrum absorption. These models predict the perovskite band gap using the composition and inherent elemental properties as descriptors. Eventually enabling accurate prediction and screening of the much larger chemical space from which the data samples were drawn.

I utilized a recently published density functional theory (DFT) dataset of more than 1300 perovskite band gaps from four different levels of theory, added to an experimental perovskite band gap dataset of ~ 100 points, to train random forest regression (RFR), Gaussian process regression (GPR), and Sure Independence Screening and Sparsifying Operator (SISSO) regression models, with data fidelity added as one-hot encoded features. I found that RFR yields the best model with a band gap root mean square error of 0.12 eV on the total dataset and 0.15 eV on the experimental points. SISSO provided compound features and functions for direct prediction of band gap, but errors were larger than from RFR and GPR. Additional insights gained from Pearson correlation and Shapley additive explanation (SHAP) analysis of learned descriptors suggest the RFR models performed best because of (a) their focus on identifying and capturing relevant feature interactions and (b) their flexibility to represent nonlinear relationships between such interactions and the band gap. The best model was deployed for predicting experimental band gap of 37785 hypothetical compounds, based on which we identified 1251 stable compounds with band gap predicted to be between 1 and 2 eV at experimental accuracy. Successfully narrowing to about 3% of the screened compositions.

1. INTRODUCTION

Perovskites have historically been materials of great interest for a variety of optoelectronic applications with special interest in the past ten years (see figure 1.1) in their potential as photovoltaic absorbers. (Ansari et al., 2018; Brenner et al., 2016; Manser et al., 2016; Yin et al., 2015) A cubic phase perovskite unit cell with general formula ABX_3 contains two cations A and B at the corners and body center, and an anion X at each of the face centers. The symbolic 3D perovskite structure is a network of BX_6 octahedra robustly held together by large A-site cations. This unique structure means that perovskite properties are highly tunable by changing the size and number of A/B/X species, by manipulating relative octahedral arrangements, and by creating non-cubic and metastable phases. Halide perovskites (HaP), as opposed to the oxide perovskites that have been well researched over the past century are so characterized because their X-site anions are halogens. Their B-site cations may be divalent elements, and the A-site is occupied by large monovalent cations that are either inorganic elements or organic molecules.

The most commonly studied hybrid organic-inorganic HaPs, $MAPbI_3$ and $FAPbI_3$, have demonstrated large power conversion efficiency (PCE) values between 20% and 25% when used as absorbers in single- or multi-junction solar cells. (Cui et al., 2019; Jeong et al., 2020) This is a five-fold improvement over the efficiencies of the same compositions first reported in 2009 and demonstrates the most attractive feature of HaPs, their unique tunability. A theoretical cubic perovskite structure is considered stable if the ionic radii of A, B, and X-site species satisfy the well-known tolerance (t) and octahedral (o) factors. (Bartel Christopher et al., 2019) Even accounting for stability constraints, the chemical space of perovskites experiences combinatorial scaling with the number of candidate elements which could be incorporated at each site. This poses a multidimensional optimization problem for which determining the optimal atomic fractions for a particular performance target requires data-driven acceleration. My research focused on the development and application of these design methods in the composition space of halide perovskites. The majority of work presented in this dissertation has been previously published or will be submitted for publication (See CONTRIBUTIONS).

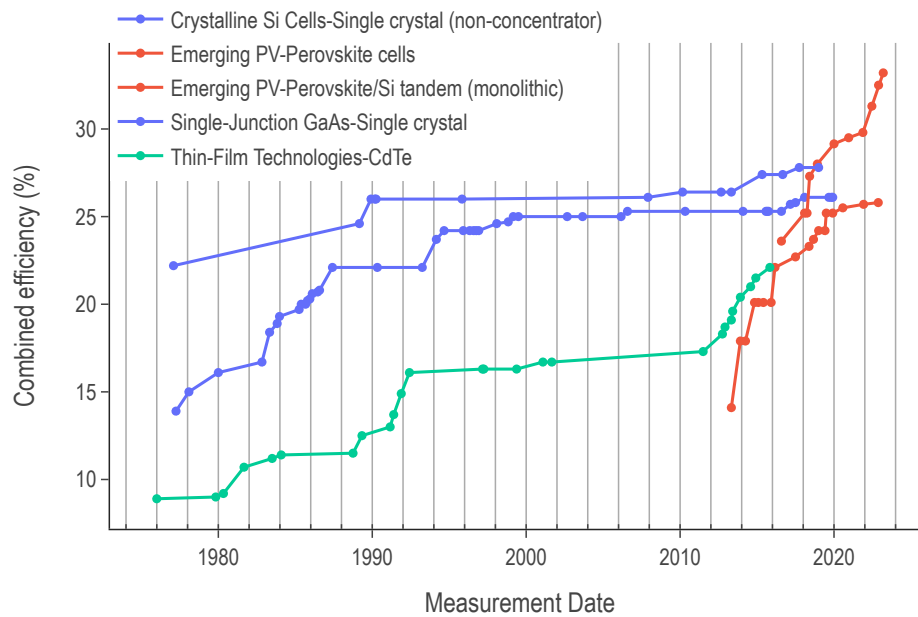


Figure 1.1. Rapid rise in cummulative maximum of HaP PCEs

1.1 Design Goals and Challenges in Perovskite PV Absorbers

Perovskite properties may be tuned in various ways. The introduction of dopants and defects (Dahliah et al., 2021; S. Kim et al., 2020) and the mutation of their cubic structure (Kar & Körzdörfer, 2018; C. Kim et al., 2017) are each promising areas of design. However, the work presented here focuses specifically on the identification of a reasonable number of candidate compositions for future laboratory trials. The most promising HaP compositions for PV absorption explored to date usually contain a mix of MA, FA, and Cs at the A-site, primarily Pb at the B-site with minor fractions of other divalent cations such as Sn and Ge, and I or Br at the X-site often with little Cl. Discovery of novel HaP compositions with attractive properties is on the rise as researchers expand the search into more complex alloys, novel A-site organic molecules, and substitutes for Pb at the B-site from Group IV, Group II, or transition elements. (Banerjee et al., 2019; Ding et al., 2019; Greenland et al., 2020; Zhu et al., 2019) Mixing at A site has been shown to improve formability (Zhang et al., 2019), while B site and X site mixing can tune and optimize band gaps and optical absorption. The allure of A/B/X-site mixing, even the creation of high entropy perovskite alloys, is in the promise to obtain dramatically different properties than those of pure compositions. Perovskite properties have demonstrated highly nonlinear responses to changes in composition. It is hoped that exploiting this could lead to possibly eliminating toxic lead, reducing degradation under light exposure, and even improving resistance to adverse environmental conditions while also targeting specific optoelectronic performance markers.

The chemical design space of HaPs is intractably large to effectively screen by physical laboratory methods. The halide perovskite chemical space covered by this dataset was based on fourteen species commonly appearing in study of these materials. The five constituents making up the A-site occupants include three inorganic and two organic cations, namely CH_3NH_3^+ Methylammonium (MA) and $\text{CH}(\text{NH}_2)_2^+$ Formamidinium (FA). (Dimesso et al., 2016; Yan et al., 2016) Six divalent metals represent the possible B-site occupants and three halogen anions make up the possible X-site occupants. See table 3.2. The total number of distinct compositions possible in a $2 \times 2 \times 2$ supercell is over 207 million. Of these

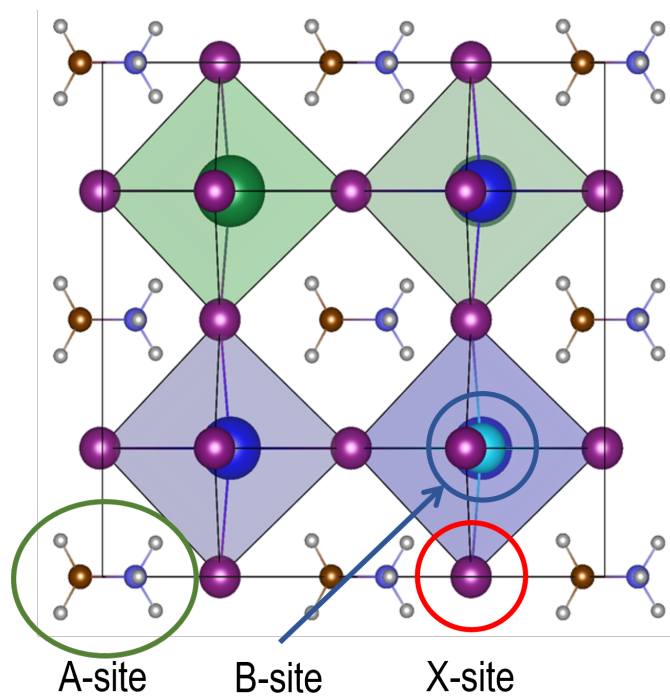


Figure 1.2. $2 \times 2 \times 2$ α -phase supercell with Methylammonium at the A-site

compositions, 37695 contain mixing at only one site and ninety are pure having no mixing at any site. I refer to the combination of these subsets as the "cardinal mixing set" and it equally represents each of the constituent species of interest. See figures 1.3 and 1.4.

First principles density functional theory (DFT) simulations have been systematically performed to study the optoelectronic properties of HaPs as a function of structure, composition, and defects. Recently, DFT simulations have been reliably used to predict structural information, band gaps, optical absorption spectra, and defect formation energies of a variety of HaPs with reasonable accuracy. (Mannodi-Kanakkithodi & Chan, 2022; Yin et al., 2015) An examination of the HaP-related computational literature reveals that there have been numerous medium ($\sim 10^2$ data points) to large ($\sim 10^3$ or more data points) DFT datasets reported for HaPs. (Castelli et al., 2014; Kar & Körzdörfer, 2018; Park et al., 2019; Pu et al., 2021) These have been successfully screened to identify promising materials with desired stability and formability as well as PV-suitable band gaps, among other properties.

A clear limitation of High-Throughput (HT) DFT driven screening is the computational expense of applying a suitably advanced level of theory across a very large number of materials. This problem is typically addressed by coupling DFT computations with machine learning (ML) techniques. Within the area of perovskites, there are many examples in the literature where DFT datasets and suitable atomic/structural/compositional descriptors have been used to train a variety ML-based predictive and classification models, leading to accelerated prediction of lattice constants, formation energies, band gaps, and other important properties. (Lee et al., 2021; Park et al., 2019; Stanley et al., 2020) Such DFT-ML models, once rigorously trained and tested, are deployed for high-throughput screening across massive sample spaces of unknown perovskites. (J. Yang & Mannodi-Kanakkithodi, 2022)

Table 1.1. ABX₃ candidate species per site

| | | | | | | |
|--------|----|----|----|----|----|----|
| A-site | MA | FA | Cs | Rb | K | |
| B-site | Pb | Sn | Ge | Ba | Sr | Ca |
| X-site | I | Br | Cl | | | |

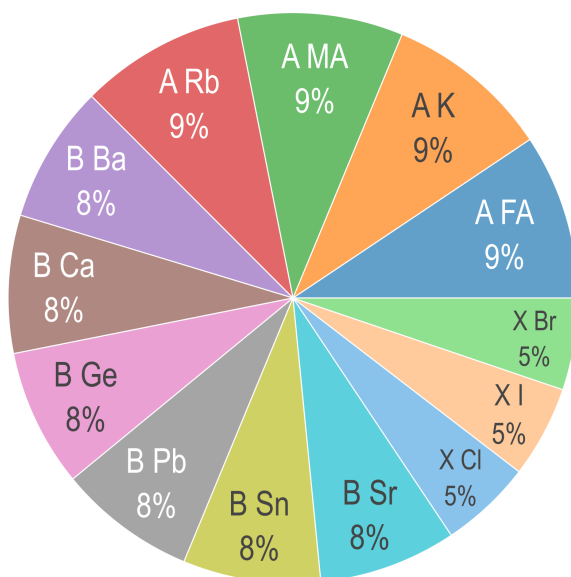


Figure 1.3. The cardinal mixing sample space contains equal fractions of each element

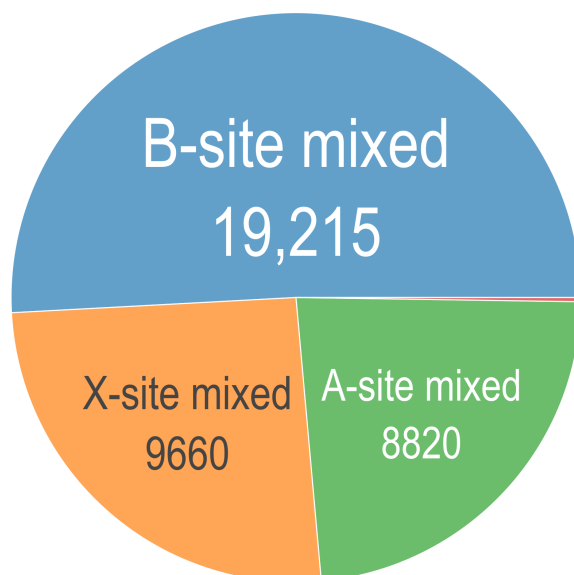


Figure 1.4. The cardinal mixing sample space contains mostly B-site mixed compounds

1.2 Multiple Fidelity Dataset

For my work I used a large DFT dataset collected over the past three years by my advisor and fellow student Jiaqi Yang. This dataset consists of approximately 1300 calculations based on approximately 500 chemically distinct, pseudo-cubic, halide perovskite alloys reported in the Mannodi research group’s prior work. (Mannodi-Kanakkithodi & Chan, [2022](#); J. Yang et al., [2023](#)) There are more calculations than there are distinct compositions because each composition is simulated multiple times. Also, it is supplemented by an additional ~100 points of data aggregated from reputable sources by Almora et al. ([2020](#)). In total it contends as one of the largest first principles halide perovskite datasets and represents years of work. The relatively large size of this dataset samples the space of all possible single-site mixed compositions with good coverage. This enables the training of interpolative models in the HaP composition space promising lower and less frequent error than if lesser coverage were used. In this dataset, all perovskite structures are cubic or pseudo-cubic, which aids my focus on investigating effects of composition and alloying on photovoltaic performance.

2. DENSITY FUNCTIONAL THEORY SIMULATION

All DFT computations were performed using vasp version 6.2 employing projector-augmented-wave (PAW) pseudo-potentials. (Kresse & Furthmüller, 1996a, 1996b; Kresse & Hafner, 1993, 1994; Kresse & Joubert, 1999) Multiple levels of theory (LoT) were used in most computations. Each simulation was conducted on the same set of compositions allowing *at most* single-site mixing of our 14 constituent candidates for 3 sites (table 3.2). Each HaP composition is simulated in a $2 \times 2 \times 2$ supercell, which allows A and B-site mixing to be performed in discrete $1/8^{\text{th}}$ fractions of the total site occupancy, and X-site mixing in $1/24^{\text{th}}$ fractions, though for simplicity, we restrict X-site mixing to fractions of $3x/24$. For simulating mixed perovskites, the special quasi-random structures (SQS) method was applied to build periodic structures that make the first nearest-neighbor shells as similar to the target random alloy as possible. (Z. Jiang et al., 2016) The final tally of successfully converged calculations is listed in table 3.1. The Perdew-Burke-Ernzerhof (PBE) functional within the generalized gradient approximation (GGA) as well as the hybrid Heyd-Scuseria-Ernzerhof functional with parameters ($\alpha = 0.25$) and ($\omega = 0.2$) (HSE06) are used for exchange-correlation energy. (Heyd et al., 2003; Perdew et al., 1996) The energy cutoff for the plane-wave basis is set to 500 eV. For all PBE geometry optimization calculations, the Brillouin zone was sampled using a $6 \times 6 \times 6$ Monkhorst-Pack mesh for unit cells and a $3 \times 3 \times 3$ for supercells. Using the PBE optimized structure as input, the electronic band structure is calculated along high-symmetry k-points to obtain accurate band gaps, and the optical absorption spectrum is further calculated using the LOPTICS tag, setting the number of energy bands to 1000 for each structure. (Ganose et al., 2018; Hinuma et al., 2016) For HSE calculations, geometry optimization was performed using only the Gamma point, and subsequent computations used a reduced $2 \times 2 \times 2$ Monkhorst-Pack mesh. The force convergence threshold is set to be -0.05 eV/Å. Spin-orbit coupling (SOC) is also applied to two flavors of HSE computations using the LORBIT tag and the non-collinear magnetic version of VASP 6.2. (Steiner et al., 2016) Optical absorption spectra from different HSE functionals were obtained by using the difference between the respective PBE and HSE band gap, and shifting the PBE-computed spectrum.

Table 2.1. Sample counts by density functional represented in dataset

| | LoT |
|-----------------|------|
| PBE | 492 |
| HSE | 297 |
| HSE(SOC) | 282 |
| HSE-PBErel(SOC) | 244 |
| EXP | 90 |
| | 1405 |

2.1 DFT Computed Band Gaps

Four types of electronic band gaps were computed by my advisor and group members using a $2 \times 2 \times 2$ Monkhorst-Pack mesh. These four measures $E_{\text{gap}}^{\text{PBE}}$, $E_{\text{gap}}^{\text{HSE}}$, $E_{\text{gap}}^{\text{HSE(SOC)}}$, and $E_{\text{gap}}^{\text{HSE-PBEl(SOC)}}$ populate the multiple fidelity dataset I model. I aim to accurately predict performance-relevant halide perovskite (HaP) band gaps, which strongly predict photovoltaic performance. (Mannodi-Kanakkithodi et al., 2019) Furthermore, using multi-fidelity modeling, I aim to predict the experimentally measured band gaps of entirely hypothetical compounds, either only ever simulated or not tested at all. This is motivated by a relationship known to exist between the absorption spectra/PCE of the simulated compounds and their band gaps.

2.2 Spectroscopic Limited Maximum Efficiency (SLME)

Introduced by Yu and Zunger (2012), the SLME is a convenient metric for evaluating a semiconductor’s suitability for single junction photovoltaic (PV) absorption. In this work, SLME is calculated considering a 5 μm sample thickness for every perovskite using equations 2.2, 2.2, and 2.2, combining the original SL3ME.py code from Yu and Zunger (2012) with our DFT computed absorption spectra and band gaps.

$$a(E) = 1 - e^{-2\alpha(E)L}$$

Here, $\alpha(E)$ is the DFT computed optical absorption coefficient as a function of incident photon energy and L is the thickness of the absorber.

$$J = e \int_0^\infty a(E) I_{\text{sun}}(E) dE - J_0(1 - e^{\frac{eV}{kT}})$$

$$\eta = \frac{P_m}{P_{\text{in}}} = \frac{\max(J \times V)}{P_{\text{in}}}$$

To calculate SLME efficiency the current density J , the light spectrum intensity of sunlight I_{sun} , and the power P are all that is needed. Using the DFT computed optical

absorption spectrum as well as the magnitude and type (direct or indirect) of band gap as input, SLME is directly calculated using an open-source package. (Williams, 2022) This calculation is performed using all four functionals and compliments the PCE measurements at the experimental fidelity. SLME accounts for more energetic processes than the Shockley-Queisser criterion ($bg \approx 1.3$) allowing for a range of performant band gaps to be identified according to level of theory (Yu & Zunger, 2012, p.1) Experimental data (Almora et al., 2020) broadly agrees with PBE simulation, so the range of 1 to 2 eV. see figure 2.1. Also, notice that even in just the sample dataset, there are candidates with potential to overtake the state of the art absorbers reported by NREL in figure 1.1. This is propitious for the screening I conduct on the 40000 point sample space.

2.3 Improving Property Predictions using HSE06 and Spin-Orbit Coupling

For a set of selected HaP compositions, while PBE-optimized lattice constants match well with experiments, PBE band gaps are underestimated, and HSE-PBE-SOC band gaps match better with measured values. GGA-PBE computations reliably compute relaxed structures of both hybrid and purely inorganic HaPs. However, advanced levels of theory such as the HSE06 functional with and without the inclusion of spin orbit coupling (SOC) to account for the relativistic effects of heavy atoms such as Pb, are of paramount importance when it comes to simulating electronic and optical properties.

The data set I used contains a series of ~300 expensive HSE calculations across the 500 sampled compositions. These are intended to yield insight into the effects of full geometry optimization at hybrid levels of theory to those of PBE-optimized structures. Also, the effect of incorporating SOC in the calculation was examined. In review, the sample of 500 band gaps available for training predictors was supplemented by 299 calculations conducted entirely at the HSE level of theory. Furthermore, an additional 282 calculations were performed with HSE in addition to SOC, and 244 calculations were performed by running HSE(SOC) electronic structure calculations on PBE-relaxed structures.

The range of band gaps sampled by each simulation method are similar and are characterized by similar variance. the descriptive statistics of each greatly exceeds those of the

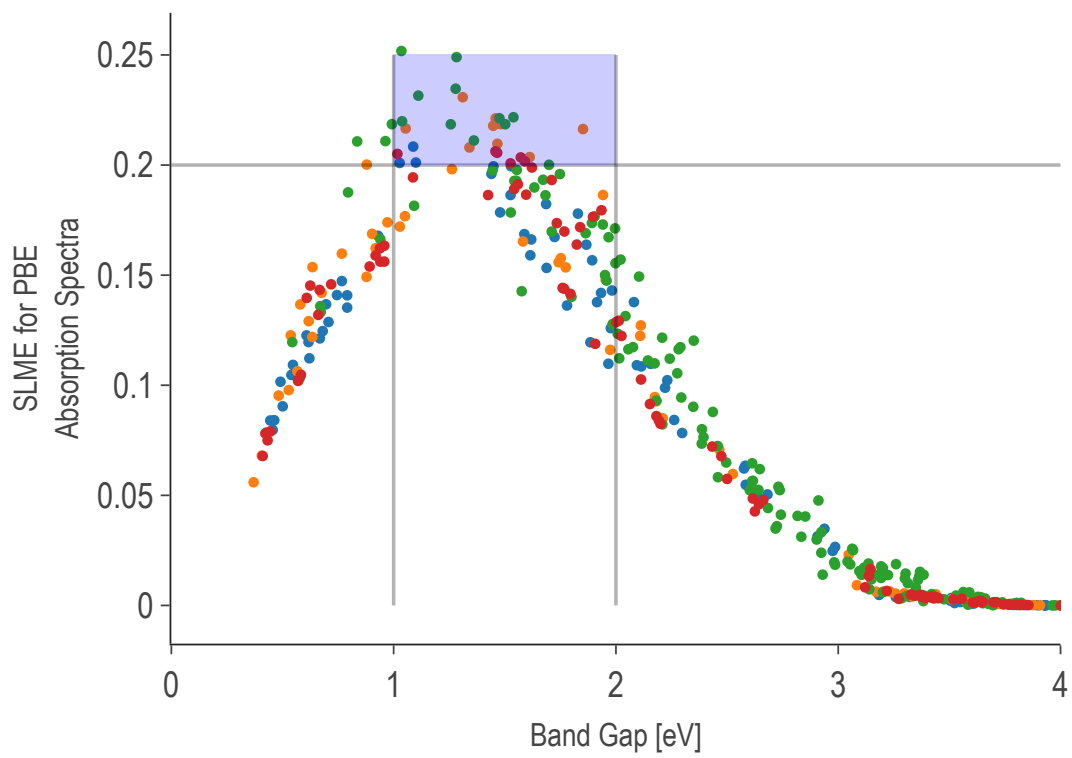
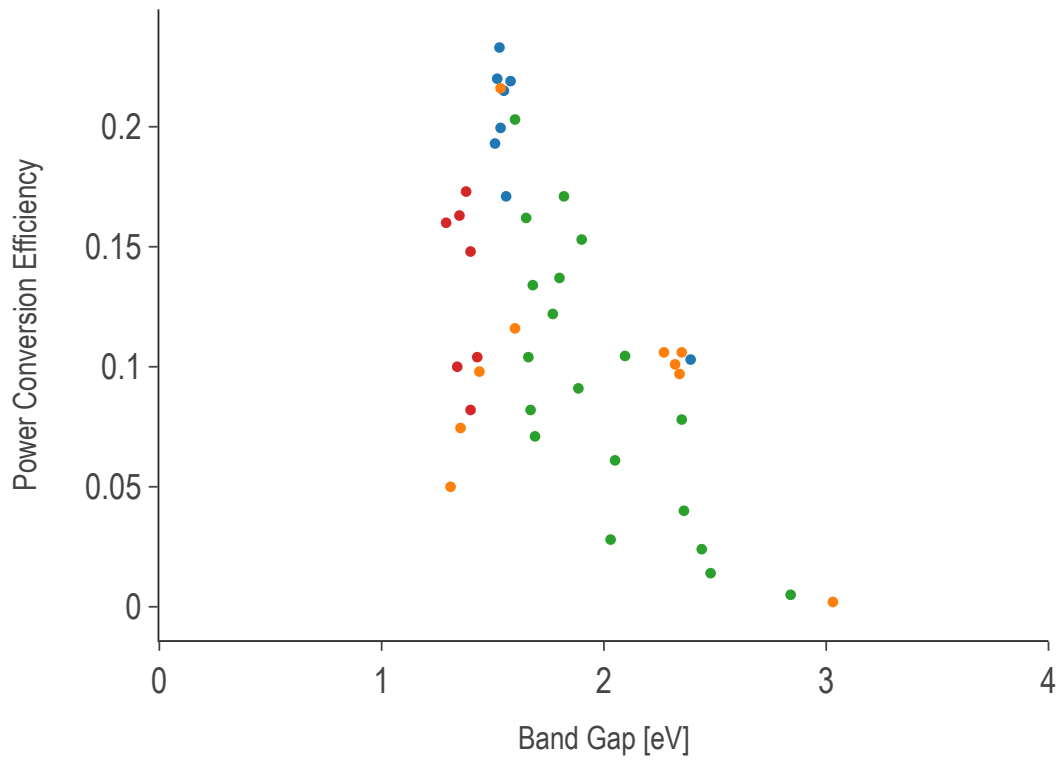


Figure 2.1. PBE SLME of sample compares to experimental PCE and cleanly demarcates competitive range of band gaps

experimental subset (see figure 3.1). Nevertheless, the latter undoubtedly represented the smallest error from truth. The types of mixing per level of theory are apportioned as in figure This is the primary challenge I address with the multi-fidelity models discussed in chapter 3.

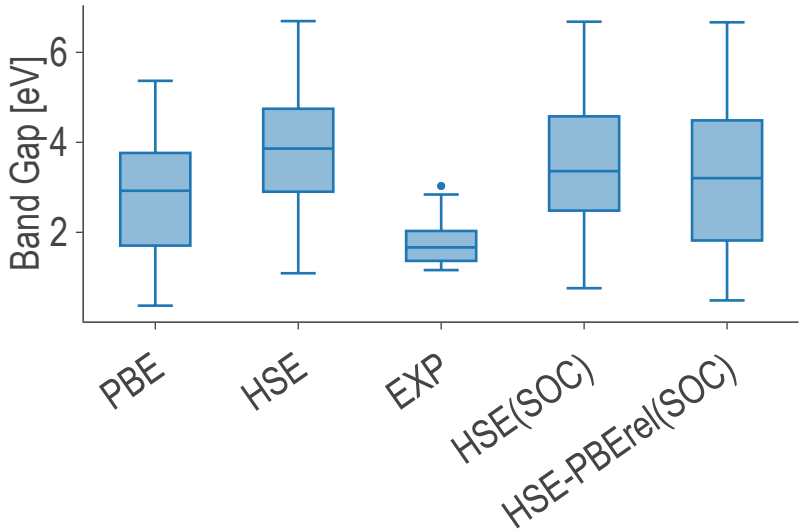


Figure 2.2. Variability in sampled band gaps at each fidelity

It is important to have a notion of which simulation is most accurate to the experimental measurements. Figure 2.3 compares the band gaps obtained for a small subset of elements at all five levels of theory. Theoretically, each functional may be more accurate for certain types of compositions. For instance, organic-inorganic perovskites might benefit from greater account of Van der Waals forces and Pb-based compounds benefit from the use of spin orbit coupling as opposed to Pb-free compounds. Note, phase information was not always available for certain experimental data points collected from the literature, and the inclusion of non-cubic phases in the tables may affect the evaluation of the functionals’ accuracy. Also, experimental data is tightly concentrated on the narrow range of performant band gaps likely due to selection bias.

The analysis is summarized in table 2.2. HSE band gaps are heavily overestimated, but may be brought down by the addition of the SOC term. Overall, HSE-PBErel(SOC) is the best approach for simulating band gaps with respect to computational cost and time. PBE RMSE is not significantly different from the HSE-PBErel(SOC) RMSE. This is due to

the accidental accuracy of semi-local functionals without SOC for hybrid organic-inorganic perovskites. (Mannodi-Kanakkithodi & Chan, 2022; Mannodi-Kanakkithodi et al., 2019)

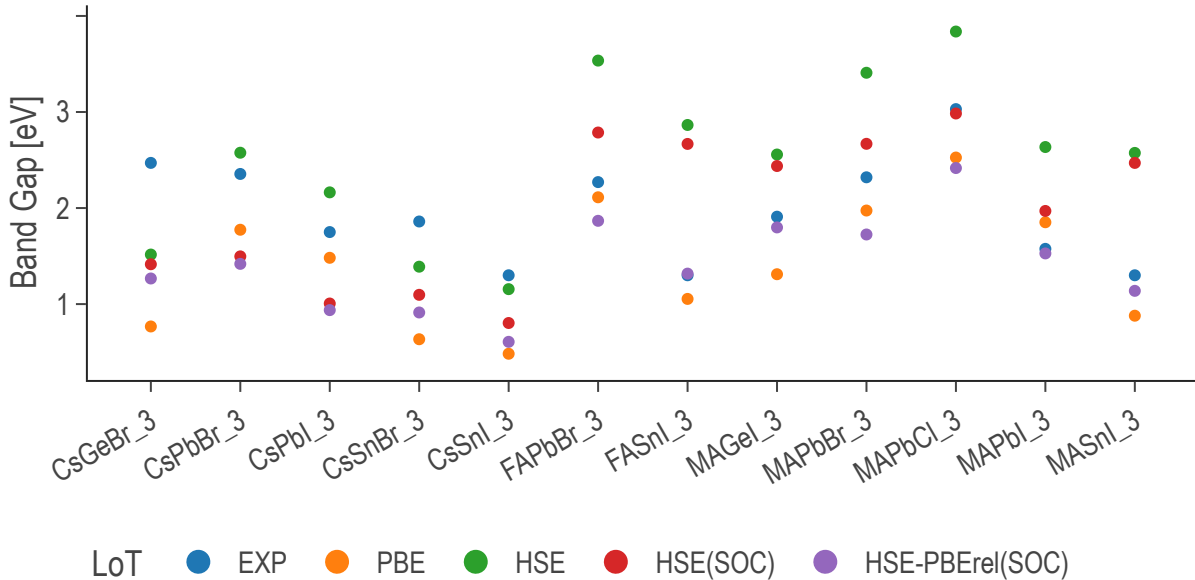


Figure 2.3. Effect of level of theory on band gap measurement

Table 2.2. RMSE values of band gaps computed from different functionals compared with experimental (Exp) values

| | RMSE vs EXP |
|-----------------|-------------|
| PBE | 0.55 |
| HSE | 0.87 |
| HSE(SOC) | 0.61 |
| HSE-PBErel(SOC) | 0.44 |

2.4 Sampling the Halide Perovskite Chemical Space

Pure (non-alloyed) possibilities are exhaustively sampled using $5 \times 6 \times 3 = 90$ compounds. Starting from these pure perovskite structures systematic mixing was performed at the A, B, and X sites. Figure 2.4 shows the shares of different types of mixing in our sample. Again, for simplicity, only cardinal mixing is considered in this study: that is, mixing is not performed at multiple A/B/X-sites simultaneously. The sample contains a reasonable balance of points

representing each one of the cardinal mixing categories. Additionally, within each mix both purely inorganic samples and hybrid organic-inorganic samples were represented equally.

See the coverage of this sample in figure 3.2.

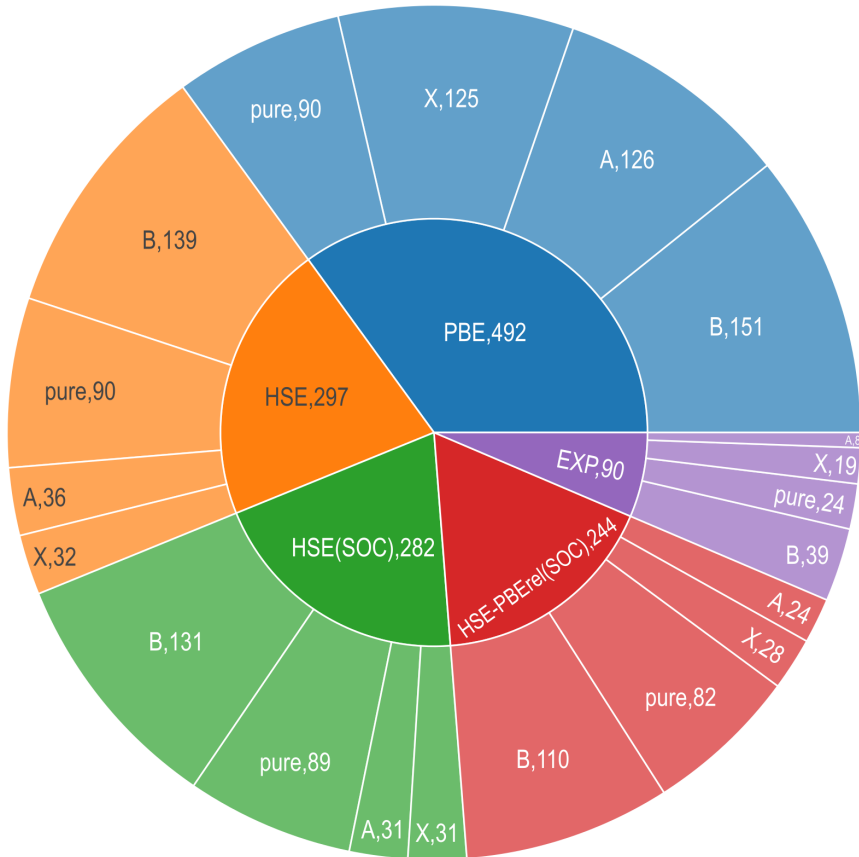


Figure 2.4. Share by count of total data apportioned from each experimental subcategory

Most importantly, this sample gives very even coverage of the cardinal mixing domain as shown in figure 3.2. The clusters in this figure are determined using the t-distributed stochastic neighbor embedding (t-SNE) method. This is a nonparametric dimensionality reduction intended for visualizing statistically relevant clusters in a high dimensional dataset in only two or three dimensions. In this case, the clusters correspond to the mix site of the member data points.

This sample provides the opportunity to comfortably interpolate the properties of other members of the cardinal mixing domain.

See Discussion.

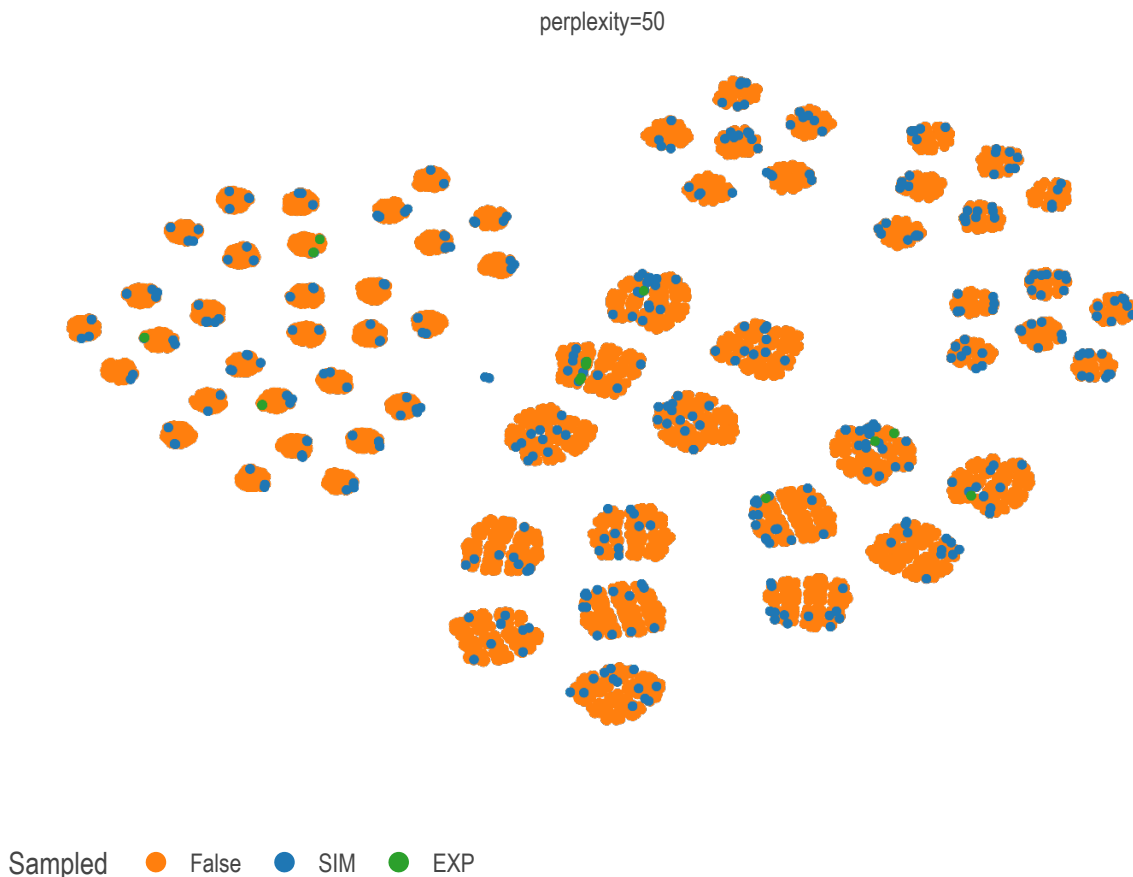


Figure 2.5. Samples overlaid on cardinal mixing chemical domain projected from fourteen to two dimensions via t-SNE

Novel halide perovskites with improved stability and optoelectronic properties can be designed via composition engineering at cation and/or anion sites. Data-driven methods, especially involving high-throughput first principles computations and subsequent analysis based on unique materials descriptors, are key to achieving this goal. I accessed a dataset consisting of – among other characteristic properties – simulated band gaps of a representative sample of halide perovskites (HaP). The effects of mixing at different sites is described by the explicit fraction of a site occupied by a specific atomic or molecular species. Also, a set of abstract features obtained as the weighted averages of these species’ bulk physical properties is used to bolster the feature space.

Our multi-objective, multi-fidelity, computational halide perovskite alloy dataset is one of the most comprehensive to date. It is publicly available in the hopes further physical and engineering insights can be extracted by the broader research community.

3. Multi-fidelity Machine Learning for Perovskite Band Gap Predictions

3.1 Multi-Fidelity Learning

The state of the art in materials modeling favors Graph Neural Network (GNN) architectures. (Chen et al., 2019; Choudhary & DeCost, 2021; Xie & Grossman, 2018) These deep learning models have sufficient flexibility to capture the continuous variability in relative positions of crystals and molecules. They are effective models, but they are difficult to use with physical materials. Accurately characterizing structures at a level of atomic granularity cannot be achieved even with state of the art 3D Electron Tomography techniques. (Ercius et al., 2015) Yet, characterization of chemical composition is a well established practice, for example using X-ray spectroscopy.

Graph convolutional neural networks can power more accurate structure-target predictions at multiple fidelities (Chen et al., 2020) by performing Multi-Task Learning (MTL). For instance, this multiple-fidelity machine learning technique can infer the relationships between more plentiful PBE GGA data and rarer but more accurate HSE06 data based on a shared set of predicting features. This relationship, if sufficiently general, can be used to reliably extrapolate from known points on the PBE co-domain to the unknown HSE co-domain. Of course, while this is implemented successfully in neural networks, the concept holds for any model architecture that can simultaneously regress multidimensional targets which do not need to constitute one rectangular data structure.

Additionally, there are alternative approaches for learning from multiple fidelities of data that can be implemented on the domain side. This circumvents the requirement for flexibility in encoding the co-domain. For instance modeling the multiple outcomes as varying depending on a categorical variable representing the fidelity makes it possible to use a single target regression methods. Our problem of accurately modeling low availability, high fidelity targets is approached in this way.

We will employ the domain-side approach where the largest, lowest fidelity component of our dataset consists of density functional theory (DFT) band gap predictions made at the generalized gradient approximation (GGA) Perdew-Burke-Ernzerhof (PBE) level of

theory. On the other end, the smallest and highest fidelity subset of the sample consists of experimental measurements of physical devices collected from the literature.

3.2 Multiple Fidelity Dataset

3.2.1 Perovskite Band Gaps

We aim to accurately predict performance-relevant halide perovskite (HaP) band gaps, which strongly predict photovoltaic performance. (Mannodi-Kanakkithodi et al., 2019)

Furthermore, using multi-fidelity modeling we aim to predict the experimentally measured band gaps of compounds that have only been simulated to date. Our fidelity hierarchy climbs from DFT simulations performed using the basic PBE GGA functional, to results obtained from physical experiments aggregated in literature see table 3.1. (Almora et al., 2020; J.-P. Kim et al., 2014; Swanson et al., 2017)

While we acknowledge the advantages of GNNs, we aim to express band gap as functions primarily of the perovskite composition. It is known the octahedral arrangement of perovskites is most relevant to their electronic structure, nevertheless, a strong understanding of the influence of chemical composition on performance will continue to be a priority as it is expected to aid in [Feature Engineering](#).

Table 3.1. Sample counts by density functional represented in dataset

| | LoT |
|-----------------|------|
| PBE | 492 |
| HSE | 297 |
| HSE(SOC) | 282 |
| HSE-PBErel(SOC) | 244 |
| EXP | 90 |
| | 1405 |

A detailed analysis of this combined hybrid organic-inorganic and purely inorganic HaP DFT dataset is covered in a prior article by J. Yang and Mannodi-Kanakkithodi (2022) and in 3.3.1. Naturally, the statistics obtained from each fidelity vary (figure 3.1). This is the primary challenge we will address with the categorically dimensioned multi-fidelity models discussed in 3.3.

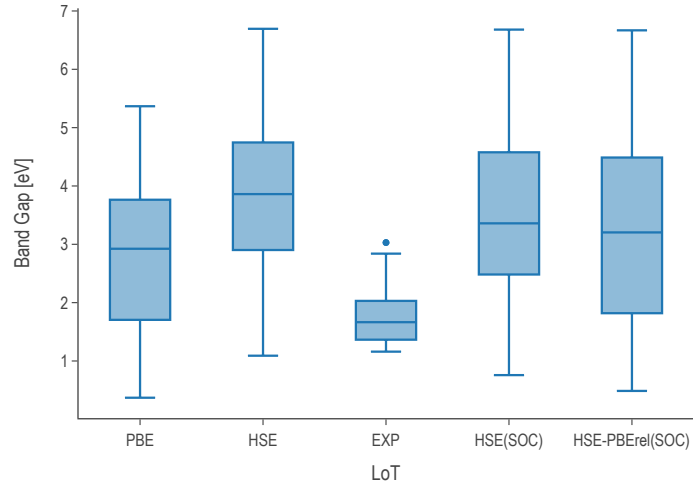


Figure 3.1. Variability in band gaps at each fidelity

3.2.2 Sampling

The simulations for each level of theory are performed on some number of members to a fixed subset of the total 37785 compositions that can be combinatorially generated in a 2x2x2 perovskite supercell when allowing *at most* single-site alloying with our 14 constituent candidates for 3 sites (table 3.2).

Table 3.2. ABX₃ Chemical Domain

| | | | | | | |
|--------|----|----|----|----|----|----|
| A-site | MA | FA | Cs | Rb | K | |
| B-site | Pb | Sn | Ge | Ba | Sr | Ca |
| X-site | I | Br | Cl | | | |

Within this domain space, we try to maintain a balance in the share of samples that represent each one of the "cardinal mixing" categories. Additionally, within each mix we try to maintain a reasonable balance of purely inorganic samples versus hybrid organic-inorganic samples. See 3.3 for details on how these categories were utilized in model development.

This previously reported dataset demonstrates very even coverage of the cardinal mixing domain as shown in figure 3.2. The clusters in this figure correspond to the alloying scheme of the data points

This sample provides the opportunity to comfortably interpolate the properties of other members of the cardinal mixing domain. Concurrently, we test the ability of our models to extrapolate with respect to alloying scheme as well as level of theory. It also provides an opportunity to investigate the statistical impact of constituent compounds on perovskite property prediction. See 3.5.

3.2.3 Model Optimization

The rigorous hyper-parameter Optimization (HPO) of any feature engineering and modeling pipeline is a problem discussed extensively in the literature. HPO approaches can be broadly separated into exhaustive and efficient optimization strategies. (L. Yang & Shami, 2020) We use a two-stage procedure for selecting the best model parameters.

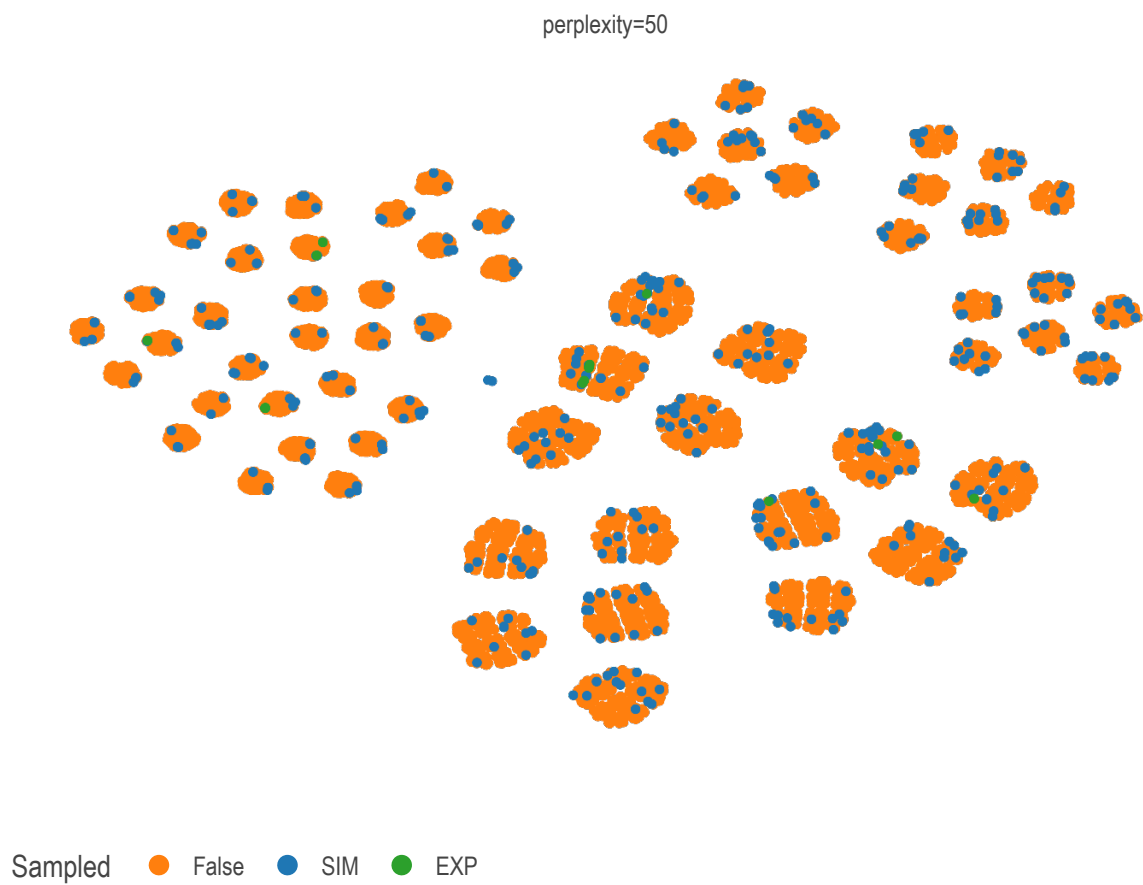


Figure 3.2. Samples overlaid on cardinal mixing chemical domain projected from fourteen to two dimensions via t-SNE

The first stage is an exhaustive grid-search over diversely sampled parameter space. Each combination of parameters instantiates a model which is then fit to each of a set of stratified training subsets generated by a K=3 K-fold split cross-validation strategy. Every fitted model is subsequently tested against the cross-validation test sets and a suite of regression scoring metrics are applied to each member category simultaneously using a custom SciKit-learn score adapter¹. The grid search is then narrowed to a high performance quadrant of the search space by the model evaluator based on recommendations made by a simple entropy minimization algorithm¹.

The recommended grid quickly eliminates under-performing settings based on the sample probability of a setting appearing in a set of finalists according to the scoring rankings. The selection score is additionally influenced by a weighted sum of the scoring ranks allowing for considerably tuning the selection criterion. For best results, a few different grid spaces should be explored to corroborate eliminations.

After the recommendation is made, the granularity of the grid is increased in the remaining ambiguous parameters and the process is repeated. In general, no more than 2 or 3 exhaustive searches are needed over a given set of grids. Past this point, continuously variable hyper parameters can be individually optimized by plotting validation curves.

3.3 Methods

3.3.1 DFT Details

The largest subdivision of 1400 compounds correspond to a series of optoelectronic DFT simulations. The simulated experiments are performed on some subset (table 3.1) of ~500, exclusively pseudo-cubic, ABX₃ supercells obtained by geometry optimization of modified structure files (Pilania et al., 2016) originally obtained from the Computational Materials Repository². Each cell demonstrates an SQS mixed composition at none or one of each of the A, B, or X sites. See the coverage of this sample in figure 3.2.

¹[↑https://github.com/PanayotisManganaris/yogi](https://github.com/PanayotisManganaris/yogi)

²[↑https://cmr.fysik.dtu.dk/](https://cmr.fysik.dtu.dk/)

Listing 3.1. An example of the cmcl "ft" feature accessor

```
import cmcl
Y = load_codomain_subset()
df = Y.Formula.to_frame().ft.comp()
df.index = Y.Formula
print(df)
```

Each relaxed structure is made in two ways. Once with the PBE GGA functional and once with the HSE06 functional. Band gaps are obtained using a static band structure calculation performed at the same and at higher levels of theory.

The chosen functionals each offer strengths and weaknesses. PBE is inexpensive but typically underestimates band gaps. HSE06 is orders of magnitude more expensive and may fail to converge structure relaxations but tends to be more trustworthy for electronic structure properties. HSE06 on PBE relaxation attempts to mitigate the disadvantages of each individually. The use of Spin Orbit Coupling helps to better electronic properties simulation in compounds containing Lead.

3.3.2 Featurization of Chemistries

For α total A-site constituents represented in the whole database, β total B-site constituents, and γ total X-site constituents, we provide a Python tool³ which robustly converts the composition string of each data point into a $\alpha + \beta + \gamma$ dimensional composition vector. In the case of our total dataset description $\alpha + \beta + \gamma = 14$. (J. Yang & Mannodi-Kanakkithodi, 2022) In a subset of the data, the chemical vector (listing 3.2) is produced using cmcl (listing 3.1).

This is naturally a sparse, relatively high dimensional descriptor. With any growth in the composition space it becomes sparser. This descriptor has been shown to be effective for interpolating the properties of irregularly mixed large supercells. (Mannodi-Kanakkithodi

³<https://github.com/PanayotisManganaris/cmcl>

Listing 3.2. Data frame of composition vectors generated by cmcl

| | FA | Pb | Sn | I | MA | Br |
|-------------------|-----|-----|-----|-----|-----|-----|
| Formula | | | | | | |
| FAPb_0.7Sn_0.3I_3 | 1.0 | 0.7 | 0.3 | 3.0 | NaN | NaN |
| MAPb(I0.9Br0.1)3 | NaN | 1.0 | NaN | 2.7 | 1.0 | 0.3 |

& Chan, 2022) However, a sparse descriptor is generally bad for extrapolative modeling. (Ghiringhelli et al., 2015)

When extrapolation is the aim, continuously distributed, unique, and linearly independent features are much more reliable. (Lux et al., 2020)

Our attempts to provide a domain with these characteristics results in the following raw feature space.

- 14 sparse composition vectors extracted from chemical formula using `cmcl`³
- 36 dense site-averaged property space computed as a linear combination of composition vectors and measured elemental properties (Mentel, 2014)
- 5 categorical dimensions one-hot-encoding level of theory.
 - this provides the categorical axis for multi-task learning
 - see table 3.1

3.3.3 Machine Learning Algorithms and Parameter Optimization

We train Random Forest Regression (RFR) and Gaussian Process Regression (GPR) models of band gap on the union of predictor features previously discussed. The RFR is a flexible nonlinear model, the GPR a principled linear model. Shapley Additive Explanation (SHAP) analysis of the models lends insight to the average physical impacts of 1) site-specific alloying and 2) using organic molecules in the Perovskite superstructure. Model development and feature extraction is performed using Python and SciKit-Learn v1.2. (Pedregosa et al., 2011)

We are careful to maintain the diversity of mixing types and hybrid-organic/inorganic samples within each fidelity subset. We expect this will help to ensure the models learn relationships between fidelities, not differences in alloy scheme or constituency distributions within each fidelity.

Each model architecture is rigorously optimized with regard to both 1) generality over the domains of Perovskite compositions and site-averaged constituent properties and 2) generality over the domain of alloy classifications.

In order to monitor for possible categorical biases effecting regressions, nine metrics are used to evaluate the performance of each model over all alloy types at every stage of the hyper-parameter optimization. This is done simultaneously, only models that perform uniformly well on all alloy types are selected.

We expect perovskites of a given alloy class and of a given hybrid-organic/inorganic status will perform significantly differently with respect to a particular application compared to perovskites of a another class or status. We attempt to make models that reasonably explain this high entropy mixing diversity by utilizing the cardinal mixing represented in our sample.

We do this by training each model using two test/train splits. First, the optimal model parameters are chosen for their performance under a random split. A minimum of 3-fold cross-validation is performed for every set of model parameters that is considered.

Finally, the optimized model’s ability to extrapolate is tested by training/testing on splits determined with a groupwise K-fol] splitting strategy.

Two separate cross validation schemes are employed at each stage of the design process. First, the sample set is shuffled once and split to mitigate the models tendency to fit on sample order, then, stratified K-folds are generated in manner consistent with the types of each sample. The regressor is then trained on the subsets of each class. Its ability to extrapolate is independently metered on each validation fold consisting of members of the other classes.

Second, the ability for a model trained on samples belonging to one class/status to extrapolate to samples of another class/status is tested as well. The samples again are shuffled and split. then the training set is separated using a grouping K-fold split strategy.

A final best model is instantiated using the overall best performing parameters. These models are finally validated against the test sets originally split off from the sample in both their extrapolative ability and consistency Thiprocedure in demonstrated in an online notebook by Manganaris et al. ([2022](#)) hosted on the Purdue NanoHUB.

3.3.4 Feature Engineering

There has been success in creating analytical expressions for perovskite properties, particularly lattice parameters. (L. Jiang et al., 2006) In an attempt to find an analytical predictor for band gap we employ the Sure Independence Screening and Sparsifying Operator (SISSO). (Ouyang et al., 2018)

SIS⁴ is a powerful application of compressed sensing. (Ghiringhelli et al., 2017) The SIS operator is a potent dimensionality reduction technique. It does not perform any mathematical decomposition but instead picks existent dimensions that begin to approximate an orthogonal basis. It outperforms CUR decomposition by functioning effectively in extremely high rank vector spaces. (Hamm & Huang, 2019; Ray et al., 2021) This is accomplished by posing the decomposition as a compressed sensing problem in the correlation metric space.

It allows the program to effectively find candidates for a linearly independent basis in a vector space of immense size. unlike legacy techniques, e.g. LASSO, it does not suffer when features are correlated. (Gauraha, 2018; Tibshirani, 1996)

This allows for it to be used in performing a brute force search of a super-space generated by combinatorial operations on the raw predictor variables.

The Sparsifying Operator finds members of the resulting basis set which correlate with the target co-domain. it does this by creating a sparsified linear model, similar again to a LASSO. This process produces an analytic model of the target property, which is easy to interpret and can even be constrained for consistent combination of dimension units.

Subsequent applications of the SIS operator to the residuals of this model are a clever interrogation of error yielding more orthogonal basis sets that can be incorporated into the model. (Mayo, 1996)

SISSO is run for our dataset on the same partitioning scheme used by the previous models via an SciKit-learn compliant (Buitinck et al., 2013) interface⁵ extensively modified from the original Matgenix⁶ code. Additionally, the algorithm is informed of features units so that it is restricted to meaningful linear combinations. SIS features complexity is restricted to

⁴[↑https://github.com/rouyang2017/SISSO](https://github.com/rouyang2017/SISSO)

⁵[↑https://github.com/PanayotisManganaris/pysisso](https://github.com/PanayotisManganaris/pysisso)

⁶[↑https://github.com/Matgenix/pysisso](https://github.com/Matgenix/pysisso)

a maximum of 3 operations primarily to encourage parsimonious descriptions. The available operation set is outlined in table 3.3.

Table 3.3. operations for formation of combinatorial super-space

| Binary | Unary |
|----------------|-------------------|
| addition | reciprocation |
| subtraction | power 2 |
| multiplication | power 3 |
| division | natural logarithm |
| | exponentiation |
| | root 2 |

3.4 Results

3.4.1 Best Models on Raw Domain

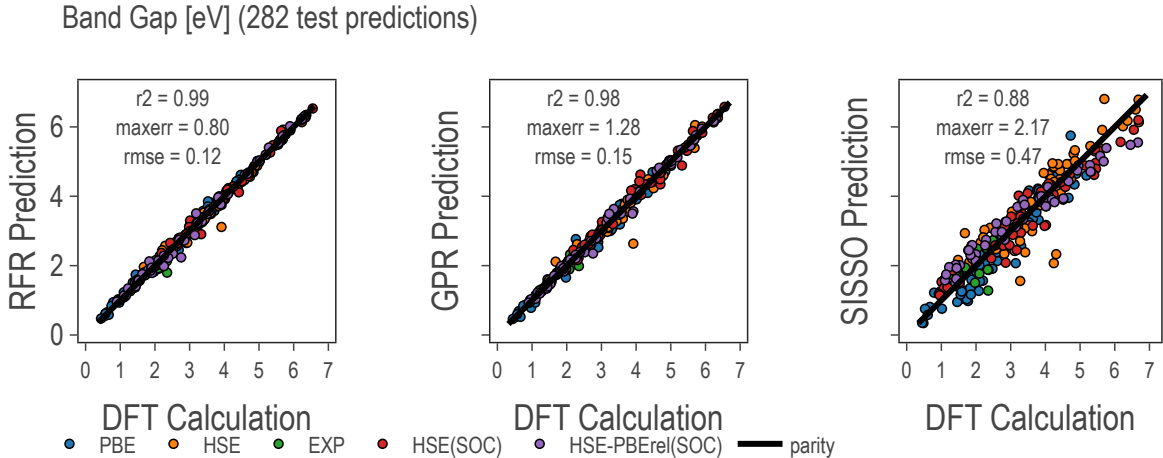


Figure 3.3. model predictions vs true values at multiple fidelities

The optimized models are high performing (Table 3.4). The RFR hyper-parameters are listed in the appendix (Table ??).

The GPR model is tried with multiple kernels. Ultimately, the best is a non stationary Matern kernel with $\nu = \frac{3}{2}$.

3.4.2 SISSO Model and SIS Engineered Features

The Sure Independence Screening and Sparsifying Operator (SISSO) is a specific combination of multiple data mining techniques chained together resulting in a symbolically expressed regression model. (Ghiringhelli et al., 2017; Ouyang et al., 2018)

The best SISSO model for band gap involving 3 SIS features (each composed of up to 4 basic features) has an unremarkable RMSE of 0.476 eV, barely outperforming an OLS regression on 55 dimensions (see Table 3.4). It is expressed in equation 3.1. Notably, while the units of the expression do not match the units of band gap as measured (target units are unknown to the algorithm), they are still energy units. This is by design, as the combination of features was restricted so to only allow compatible units to be combined. A separate training session without this restriction was attempted, but the resulting model’s performance was worse.

$$\begin{aligned}
 bg \text{ [eV]} = & 1.752393064((X; \text{electronegativity} * A; \text{heat of fusion}) - (B; \text{electron affinity} + B; \text{ionization energy})) \\
 & + -0.5862929089((B; Sn - \text{HSE}) + (\text{PBE} - X; \text{electronegativity})) \\
 & + 1.063684923((A; \text{electronegativity} - B; Ca) * (B; \text{heat of vap} - X; \text{electron affinity})) \\
 & + 4.657097107
 \end{aligned}
 \tag{3.1}$$

Table 3.4. RMSE of models on raw domain calculated per LoT subset

| Score Categories | GPR | RFR | Linear OLS | SISSO | SIS + GPR | SIS + RFR |
|-------------------|----------|----------|------------|----------|-----------|-----------|
| rmse | 0.156214 | 0.124738 | 0.499558 | 0.474754 | 0.251881 | 0.187431 |
| rmse EXP | 0.120475 | 0.154448 | 0.307186 | 0.330080 | 0.338949 | 0.235397 |
| rmse PBE | 0.128211 | 0.101872 | 0.472430 | 0.395827 | 0.171640 | 0.134529 |
| rmse HSE | 0.214920 | 0.152479 | 0.558077 | 0.519706 | 0.305443 | 0.208390 |
| rmse HSE(SOC) | 0.156785 | 0.108867 | 0.535087 | 0.572644 | 0.272158 | 0.221007 |
| rmse HSE-PBE(SOC) | 0.130696 | 0.133027 | 0.466364 | 0.470758 | 0.252624 | 0.189510 |

Computing and combining more than 3 SIS features is not rewarding of the computational expense. Residuals are increasingly uncorrelated with the generated SIS features and model accuracy gains do not outstrip complexity. However, in the process of creating Equa-

tion 3.1, 150 SIS predictor variables were determined and recorded. 50 primary predictors, 50 first residual predictors, and 50 second residual predictors. These can serve as a high quality, introspective domain for the other architectures to fit on.

3.4.3 Best Models on Engineered Domain

We set the aim of decreasing $\mathcal{O}(n^3)$ computational expense of GPR by ≈ 10 times. So, we aim to take 30 highly correlated features (slightly more than one half the number used by prior models) from these SIS subspaces. We expected this to solve the problems inherent to the raw 3.3.2.

fitting models to SIS features may leverage the denser and more continuous domain to improve extrapolative predictions. Potentially into the high-entropy domain, or simply Theory. However using the SIS subspaces in this way compromises on SISSO’s explicability and necessitates SHAP analysis. Unfortunately, whatever the gains in training time complexity and extrapolative ability, the models underperformed in predicting band gap in the cardinal mixing domain (see Table 3.4). This was unexpected considering the raw features are by their nature highly correlated and presumed redundant. Nevertheless, the RFR model on the higher dimensional, sparser raw features is superior.

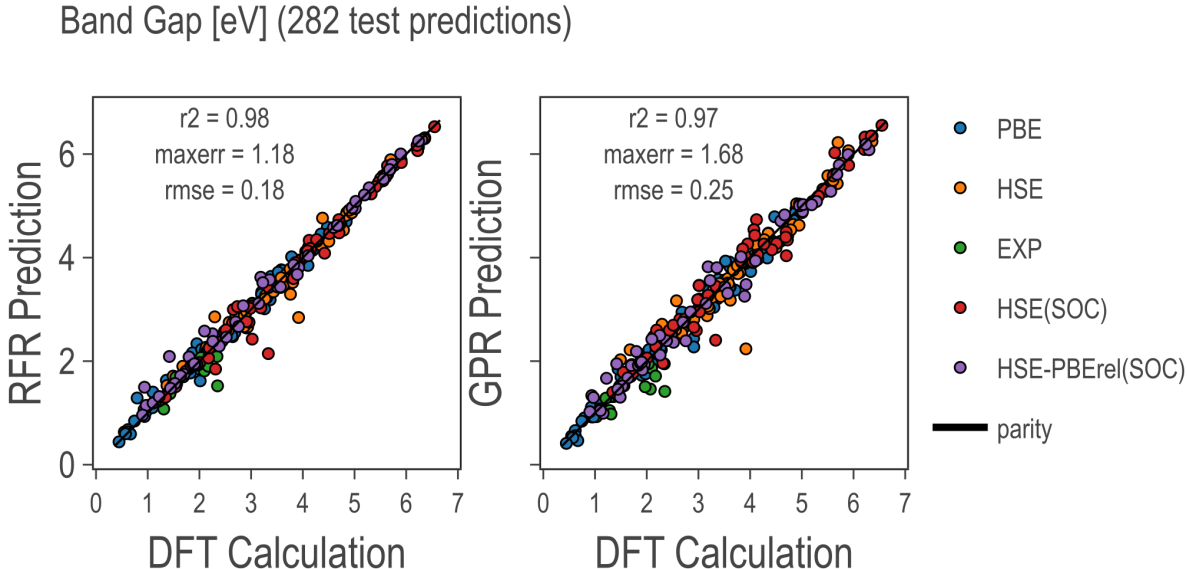


Figure 3.4. SIS-based model predictions vs true values at multiple fidelities

3.5 Discussion

3.5.1 SHAP Analysis of Domain

SHAP scores are computed automatically for every dimension of every sample in the domain by the python SHAP package⁷. The sum of the expectation value of the target conditioned on the model features and the SHAP scores computed for each predictor variable of a sample is the model’s prediction for that sample target. (Lundberg & Lee, 2017) For the perovskite band gap the expectation value is 2.836 when conditioned on the raw features and 2.863 when conditioned on the SIS features. The raw features’ SHAP values are more centered around zero while engineered features are more often scored decisively positive or negative.

Figures 3.5 and 7 show the top score distributions. In each figure, features are ranked by overall value on the y-axis. The x-axis shows the SHAP score for each point. The points are shaped in a violin plot to show the distribution of effects the presence of the given feature can have. Finally, on the color-axis, feature value specifies whether a particular score is a large or small absolute contributor of the sum to the prediction.

For instance, in figure 3.5, the B-site Electronegativity is often a strongly positive contributor to the RFR prediction. However, almost always in this case it is out-contributed by other features, it does not mostly determine the result but it is still valuable. On the contrary, when it is a strongly negative contributor it effectively determines the result. It is interesting to see how models make use of features in light of basic bi-variate correlations. The only features that correlate strongly with band gap are illustrated in figure 3.7. Notably, the Random Forest Regression (RFR) primarily uses the highly correlated features, while the Gaussian Process Regression (GPR) primarily uses features with lower Pearson correlations.

SHAP scores in principle quantify the contributions of site members and site member properties to the perovskite band gap. On a sample-by-sample basis it is possible to say how much of the bandgap is contributed by the presense of a given quantity of, for example, Germanium. However a clustering analysis reveals no universal patterns. SHAP scores given the raw domain are near zero on average regardless of partitions made by level of theory,

⁷<https://github.com/slundberg/shap>

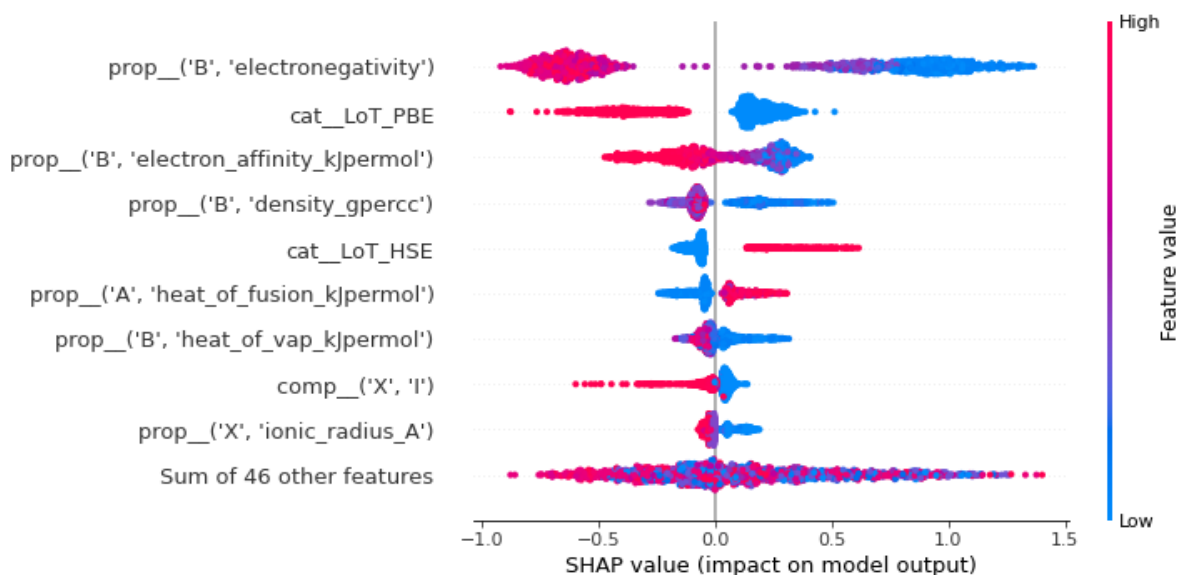


Figure 3.5. Random Forest Regression Band Gap SHAP Values

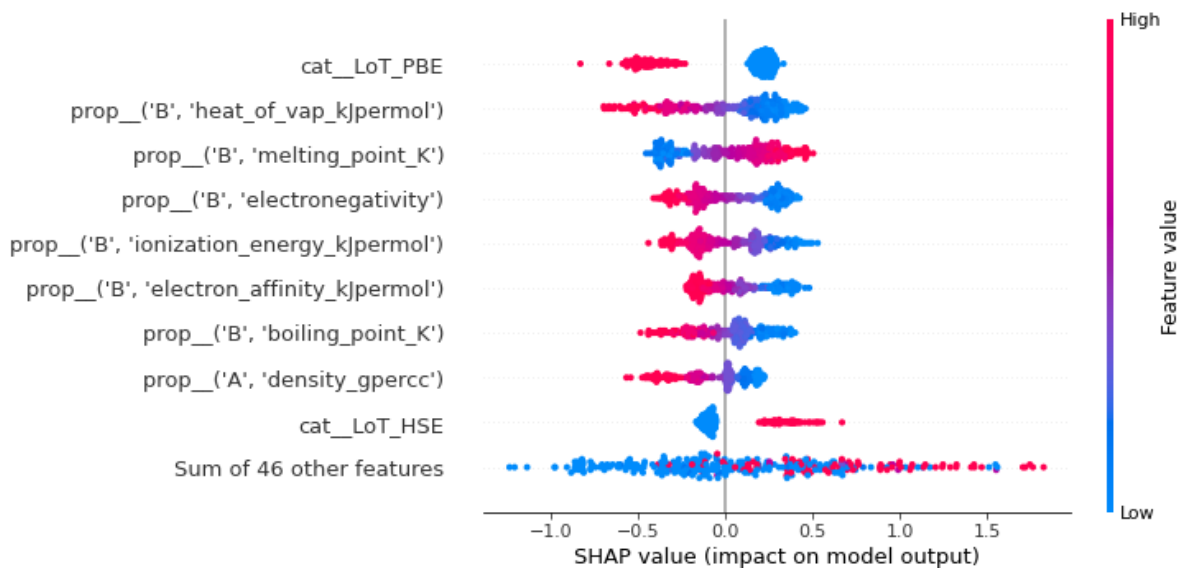


Figure 3.6. Gaussian Process Regression Band Gap SHAP Values

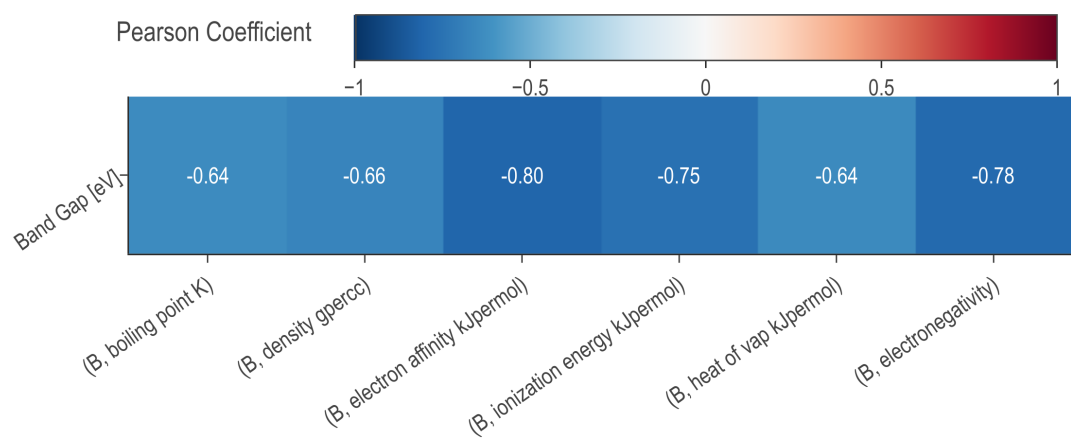


Figure 3.7. raw features with ($|p| > 0.5$) against band gap

alloy scheme, or presence of organic A-site occupants. This analysis confirms the difficulty of deducing a rule of thumb for the synthesis of perovskites with desirable properties. If anything, figure 3.8 confirms that the Iodine at the X site tends to slightly increase band gaps.

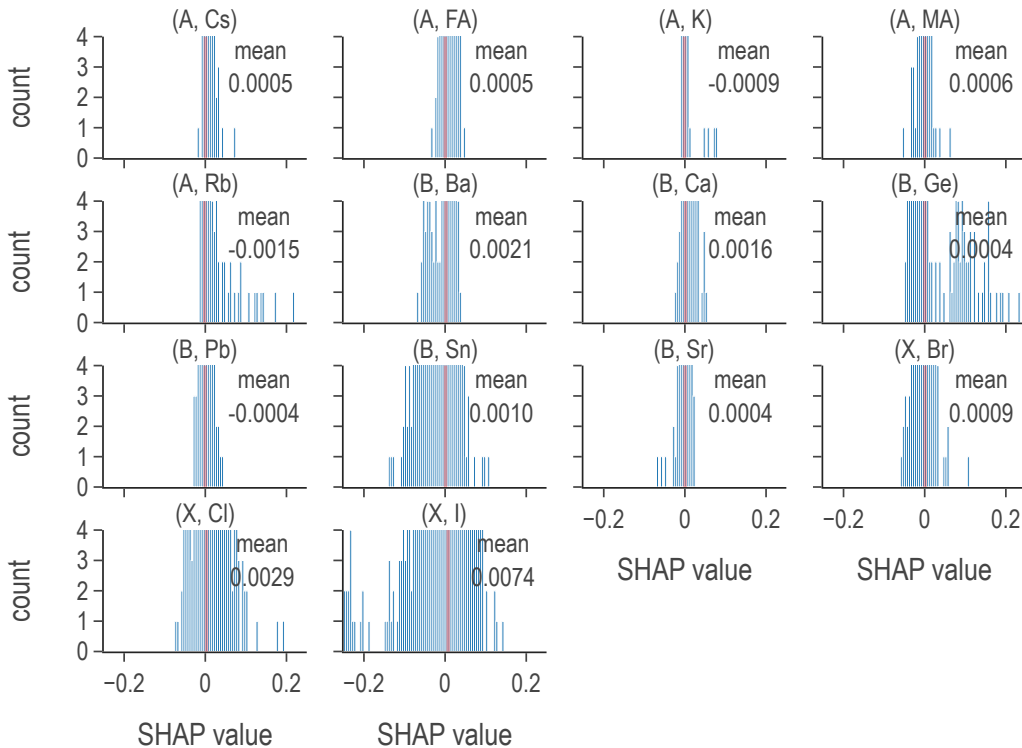


Figure 3.8. SHAP score distributions reveal effects of individual constituents

3.5.2 Predictions and Screening

Using the superior RFR model, we made predictions of the band gap for all 37785 possible compositions demonstrating cardinal mixing within the bounds of a 2x2x2 perovskite super cell. That is eight A-sites shared by up to 5 constituents, 8 B-sites shared by up to six constituents, and 24 X-sites shared by up to 3 constituents. Given the good coverage achieved by our sample dataset (figure 3.2) and according to the scores reported in Table 3.4, the RFR model is capable of predicting band gaps at the experimental fidelity with a

0.154448 rmse. (J. Yang et al., 2023) These predictions were projected on the sample space in Figure 3.9.

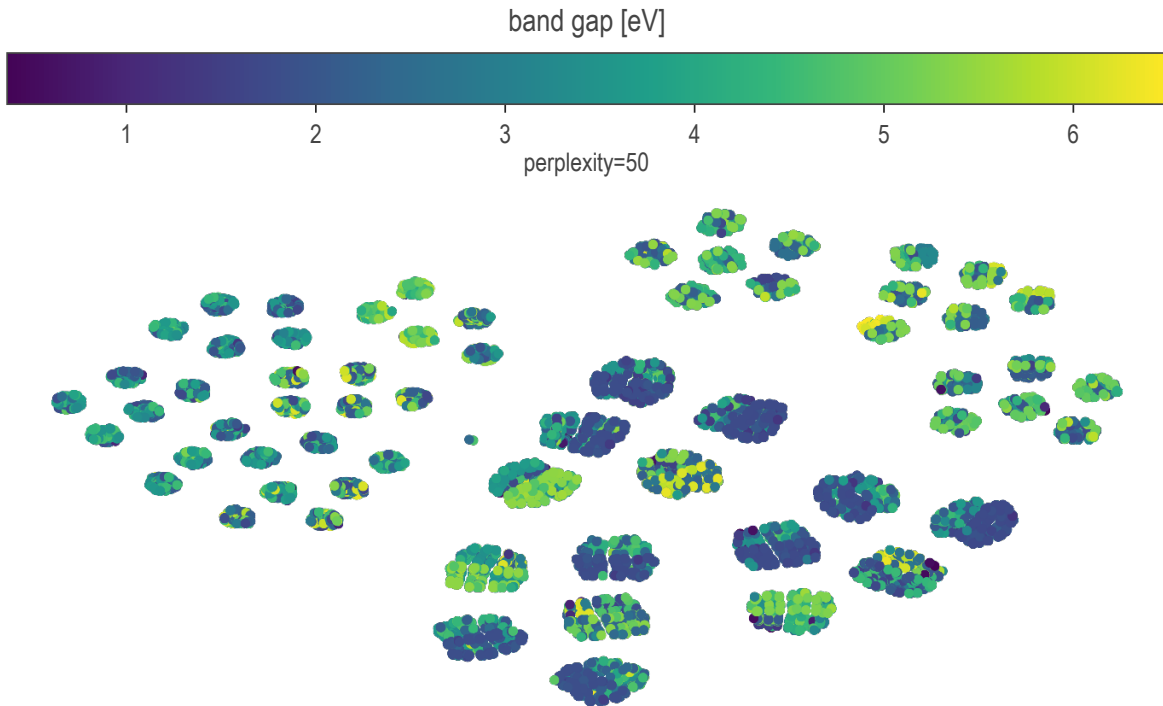


Figure 3.9. Band gap predictions overlaid on cardinal mixing chemical domain projected from fourteen to two dimensions via t-SNE

We followed a similar high-throughput screening procedure to that laid out in prior works. (Mannodi-Kanakkithodi & Chan, 2021; J. Yang et al., 2023) We selected for band gaps between 1.0 and 2.5 eV as this range is expected to yield the best power conversion efficiency (PCE) in the visible spectrum. (Shockley & Queisser, 1961; Yu & Zunger, 2012) Perovskite compounds were selected for their predicted stability by cutting on each of three tolerance factors. Namely the Goldschmidt’s tolerance, the octahedral tolerance, and the tolerance proposed by Bartel Christopher et al. (2019).

These cuts trimmed the data set from ~ 40000 points to a subset of 3247 viable candidates. These selected candidates were projected onto the domain space in Figure 11. A

Frequency analysis revealed the constituent elements of the chosen subset most often occupied either small or large shares of their site. Most A-site constituents preferred occupying $1/8^{\text{th}}$ of their site at a rate of about 8%, with Potassium and Rb also preferring full occupancy 10-12% of the time. B-site constituents favored pure configurations at a rate of 5-8% but also showed some preference for doping configurations. X-site constituents, however showed very strong preference for fully occupying their site 25% of the time. See figure 3.10.

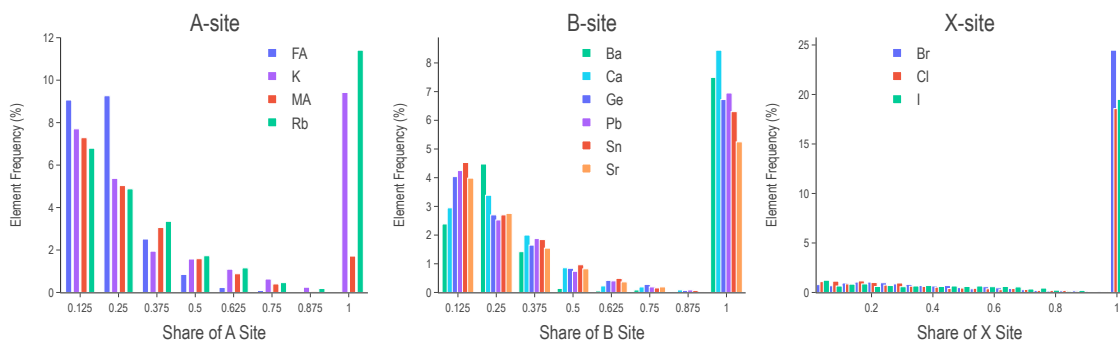


Figure 3.10. Frequency of mixing fractions of species at the A, B, and X sites across the ~3000 screen compounds

4. PUBLICATIONS

- Edlabadkar, R., Yang, J., Rahman, H., Manganaris, P., Korimilli, E. P., & Mannodi-Kanakkithodi, A. (2023). Driving halide perovskite discovery using graph neural networks [In Preparation]. <https://doi.org/00.0000/00000000>
- Gollapalli, P., Manganaris, P., & Mannodi-Kanakkithodi, A. (2023). Graph neural network predictions for formation energy of native defects in zinc blende semiconductors [In Preparation]. <https://doi.org/00.0000/00000000>
- Manganaris, P., Desai, S., & Kanakkithodi, A. (2022). Mrs computational materials science tutorial. <https://doi.org/10.21981/D1J2-AR65>
- Manganaris, P., Yang, J., & Mannodi Kanakkithodi, A. (2023). Multi-fidelity machine learning perovskite composition vs band gap [In Preparation]. <https://doi.org/00.0000/00000000>
- Yang, J., Manganaris, P. T., & Mannodi Kanakkithodi, A. K. (2023). A high-throughput computational dataset of halide perovskite alloys. *Digital Discovery*. <https://doi.org/10.1039/d3dd00015j>

5. PRESENTATIONS

- Poster for DS02 symposium MRS fall 2022
- Talk for Purdue Soft Materials symposium
- Developed MRS spring 2022 tutorial hosted on nanoHUB(Manganaris et al., [2022](#))

6. SOFTWARE AND DATA CONTRIBUTIONS

6.1 Data Publication

I published the prepared sample data I used to the Materials Data Facility. It is available to download with a simple API call following installation and activation¹ of the relevant packages and applications.

6.2 Software Tools

Additionally, a few python libraries began development with this work as the authors' attempt to contribute to the larger effort by the materials science community to ease aggregation, sharing, analysis and reporting of large computational datasets.

The `cmcl` library² is under early development under tag v0.1.5. At this stage, `cmcl` strives to provide an inquisitive interface to perovskite composition feature computers in the style of the pandas API. Listing 3.1 demonstrates its use in extracting composition vectors from the formula strings identifying each compound in a dataset.

¹<https://ai-materials-and-chemistry.gitbook.io/foundry/>

²<https://github.com/PanayotisManganaris/cmcl>

Listing 6.1. How to load the Mannodi Group halide perovskites data set from the Materials Data Facility repository

```
# THIS IS PENDING
f = Foundry(
    no_local_server=True,
    no_browser=True,
    globus=True,
    index="mdf"
)
f.load("foundry_mrg_band_gaps_v1.0", globus=globus)
res = f.load_data()
X_mp, y_mp = res['train'][0], res['train'][1]
```


A library of model evaluation tools to assist with exhaustive grid search is being maintained in the `yogi` repository.³ A grid-search assistant under the `yogi.model_selection.butler` module was used to optimize the hyper-parameters of models reported here. See documentation for the various grid-narrowing strategies available.

Matgenix⁴ company initially created a SciKit-learn compliant interface to the SISSO algorithm maintained by Ouyang et al. (2018). This code was forked and modified⁵ to enable the creation of the SIS domain engineered regressions primarily by creating a custom `Function Transformer` that may be seeded with the subspace information obtained by first training a SISSO regression using the conventional interface. This was done with the expectation that the resulting model would be superior for the purposes of this work, but it is generally applicable to any other applications demanding this sort of dimensionality reduction.

6.3 Tutorials

I developed and published one tutorial on the Purdue nanoHUB for delivery in the Spring 2022 Materials Research Society conference. Manganaris, P., Desai, S., & Kanakkithodi, A. (2022). MRS Computational Materials Science Tutorial. This tutorial covered a variety of machine learning methods. It provides a detailed example of the use of `cmcl` and `yogi` in feature extraction and training multi-fidelity random forest models by score weighting respectively.

³[↑https://github.com/PanayotisManganaris/yogi](https://github.com/PanayotisManganaris/yogi)

⁴[↑https://github.com/Matgenix/pysisso](https://github.com/Matgenix/pysisso)

⁵[↑https://github.com/PanayotisManganaris/pysisso](https://github.com/PanayotisManganaris/pysisso)

REFERENCES

- Almora, O., Baran, D., Bazan, G. C., Berger, C., Cabrera, C. I., Catchpole, K. R., ErtenEla, S., Guo, F., Hauch, J., HoBaillie, A. W. Y., Jacobsson, T. J., Janssen, R. A. J., Kirchartz, T., Kopidakis, N., Li, Y., Loi, M. A., Lunt, R. R., Mathew, X., McGehee, M. D., ... Brabec, C. J. (2020). Device performance of emerging photovoltaic materials (version 1). *Advanced Energy Materials*, 11(11), 2002774. <https://doi.org/10.1002/aenm.202002774>
- Ansari, M. I. H., Qurashi, A., & Nazeeruddin, M. K. (2018). Frontiers, opportunities, and challenges in perovskite solar cells: A critical review. *Journal of Photochemistry and Photobiology C: Photochemistry Reviews*, 35, 1–24. <https://doi.org/10.1016/j.jphotochemrev.2017.11.002>
- Banerjee, A., Chakraborty, S., & Ahuja, R. (2019). Rashba triggered electronic and optical properties tuning in mixed cation-mixed halide hybrid perovskites [not free]. *ACS Applied Energy Materials*, 2(10), 6990–6997. <https://doi.org/10.1021/acsaem.9b01479>
- Bartel Christopher, J., Sutton, C., Goldsmith Bryan, R., Ouyang, R., Musgrave Charles, B., Ghiringhelli Luca, M., & Scheffler, M. (2019). New tolerance factor to predict the stability of perovskite oxides and halides. *Science Advances*, 5(2), eaav0693. <https://doi.org/10.1126/sciadv.aav0693>
- Brenner, T. M., Egger, D. A., Kronik, L., Hodes, G., & Cahen, D. (2016). Hybrid organic-inorganic perovskites: Low-cost semiconductors with intriguing charge-transport properties. *Nature Reviews Materials*, 1(1), 15007. <https://doi.org/10.1038/natrevmats.2015.7>
- Buitinck, L., Louppe, G., Blondel, M., Pedregosa, F., Mueller, A., Grisel, O., Niculae, V., Prettenhofer, P., Gramfort, A., Grobler, J., Layton, R., VanderPlas, J., Joly, A., Holt, B., & Varoquaux, G. (2013). API design for machine learning software: Experiences from the scikit-learn project. *ECML PKDD Workshop: Languages for Data Mining and Machine Learning*, 108–122.
- Castelli, I. E., García-Lastra, J. M., Thygesen, K. S., & Jacobsen, K. W. (2014). Bandgap calculations and trends of organometal halide perovskites. *APL Materials*, 2(8), 081514. <https://doi.org/10.1063/1.4893495>

- Chen, C., Ye, W., Zuo, Y., Zheng, C., & Ong, S. P. (2019). Graph networks as a universal machine learning framework for molecules and crystals. *Chemistry of Materials*, 31(9), 3564–3572. <https://doi.org/10.1021/acs.chemmater.9b01294>
- Chen, C., Zuo, Y., Ye, W., Li, X., & Ong, S. P. (2020). Multi-fidelity graph networks for machine learning the experimental properties of ordered and disordered materials. *CoRR*. <http://arxiv.org/abs/2005.04338v1>
- Choudhary, K., & DeCost, B. (2021). Atomistic line graph neural network for improved materials property predictions. *npj Computational Materials*, 7(1), 185. <https://doi.org/10.1038/s41524-021-00650-1>
- Cui, P., Wei, D., Ji, J., Huang, H., Jia, E., Dou, S., Wang, T., Wang, W., & Li, M. (2019). Planar p-n homojunction perovskite solar cells with efficiency exceeding 21.3%. *Nature Energy*, 4(2), 150–159. <https://doi.org/10.1038/s41560-018-0324-8>
- Dahliah, D., Brunin, G., George, J., Ha, V.-A., Rignanese, G.-M., & Hautier, G. (2021). High-throughput computational search for high carrier lifetime, defect-tolerant solar absorbers. *Energy Environ. Sci.*, 14, 5057–5073. <https://doi.org/10.1039/D1EE00801C>
- Dimesso, L., Quintilla, A., Kim, Y.-M., Lemmer, U., & Jaegermann, W. (2016). Investigation of formamidinium and guanidinium lead tri-iodide powders as precursors for solar cells. *Materials Science and Engineering: B*, 204, 27–33. <https://doi.org/10.1016/j.mseb.2015.11.006>
- Ding, J., Du, S., Zhou, T., Yuan, Y., Cheng, X., Jing, L., Yao, Q., Zhang, J., He, Q., Cui, H., Zhan, X., & Sun, H. (2019). Cesium decreases defect density and enhances optoelectronic properties of mixed $\text{ma}_1\text{-xcsxpbb}_3$ single crystal. *The Journal of Physical Chemistry C*, 123(24), 14969–14975. <https://doi.org/10.1021/acs.jpcc.9b03987>
- Edlabadkar, R., Yang, J., Rahman, H., Manganaris, P., Korimilli, E. P., & Mannodi-Kanakkithodi, A. (2023). Driving halide perovskite discovery using graph neural networks [In Preparation]. <https://doi.org/00.0000/00000000>
- Ercius, P., Alaidi, O., Rames, M. J., & Ren, G. (2015). Electron tomography: A three-dimensional analytic tool for hard and soft materials research. *Advanced Materials*, 27(38), 5638–5663. <https://doi.org/10.1002/adma.201501015>

Ganose, A. M., Jackson, A. J., & Scanlon, D. O. (2018). Sumo: Command-line tools for plotting and analysis of periodic *ab initio* calculations. *Journal of Open Source Software*, 3(28), 717. <https://doi.org/10.21105/joss.00717>

Gauraha, N. (2018). Introduction to the lasso. *Resonance*, 23(4), 439–464. <https://doi.org/10.1007/s12045-018-0635-x>

Ghiringhelli, L. M., Vybiral, J., Ahmetcik, E., Ouyang, R., Levchenko, S. V., Draxl, C., & Scheffler, M. (2017). Learning physical descriptors for materials science by compressed sensing. *New Journal of Physics*, 19(2), 023017. <https://doi.org/10.1088/1367-2630/aa57bf>

Ghiringhelli, L. M., Vybiral, J., Levchenko, S. V., Draxl, C., & Scheffler, M. (2015). Big data of materials science: Critical role of the descriptor. *Physical Review Letters*, 114(10). <https://doi.org/10.1103/physrevlett.114.105503>

Gollapalli, P., Manganaris, P., & Mannodi-Kanakkithodi, A. (2023). Graph neural network predictions for formation energy of native defects in zinc blende semiconductors [In Preparation]. <https://doi.org/00.0000/000000000>

Greenland, C., Shnier, A., Rajendran, S. K., Smith, J. A., Game, O. S., Wamwangi, D., Turnbull, G. A., Samuel, I. D. W., Billing, D. G., & Lidzey, D. G. (2020). Correlating phase behavior with photophysical properties in mixed-cation mixed-halide perovskite thin films. *Advanced Energy Materials*, 10(4), 1901350. <https://doi.org/10.1002/aenm.201901350>

Hamm, K., & Huang, L. (2019). Cur decompositions, approximations, and perturbations. *CoRR*. <http://arxiv.org/abs/1903.09698v2>

Heyd, J., Scuseria, G. E., & Ernzerhof, M. (2003). Hybrid functionals based on a screened coulomb potential. *The Journal of Chemical Physics*, 118(18), 8207–8215. <https://doi.org/10.1063/1.1564060>

Hinuma, Y., Pizzi, G., Kumagai, Y., Oba, F., & Tanaka, I. (2016). Band structure diagram paths based on crystallography. *CoRR*. <http://arxiv.org/abs/1602.06402v4>

Jeong, M., Choi In, W., Go Eun, M., Cho, Y., Kim, M., Lee, B., Jeong, S., Jo, Y., Choi Hye, W., Lee, J., Bae, J.-H., Kwak Sang, K., Kim Dong, S., & Yang, C. (2020). Stable perovskite solar cells with efficiency exceeding 24.8 % and 0.3-v voltage loss. *Science*, 369(6511), 1615–1620. <https://doi.org/10.1126/science.abb7167>

- Jiang, L., Guo, J., Liu, H., Zhu, M., Zhou, X., Wu, P., & Li, C. (2006). Prediction of lattice constant in cubic perovskites. *Journal of Physics and Chemistry of Solids*, 67(7), 1531–1536. <https://doi.org/10.1016/j.jpcs.2006.02.004>
- Jiang, Z., Nahas, Y., Xu, B., Prosandeev, S., Wang, D., & Bellaiche, L. (2016). Special quasirandom structures for perovskite solid solutions. *Journal of Physics: Condensed Matter*, 28(47), 475901. <https://doi.org/10.1088/0953-8984/28/47/475901>
- Kar, M., & Körzdörfer, T. (2018). Computational screening of methylammonium based halide perovskites with bandgaps suitable for perovskite-perovskite tandem solar cells. *The Journal of Chemical Physics*, 149(21), 214701. <https://doi.org/10.1063/1.5037535>
- Kim, C., Huan, T. D., Krishnan, S., & Ramprasad, R. (2017). A hybrid organic-inorganic perovskite dataset. *Scientific Data*, 4(1), 170057. <https://doi.org/10.1038/sdata.2017.57>
- Kim, J.-P., Christians, J. A., Choi, H., Krishnamurthy, S., & Kamat, P. V. (2014). Cds nanowires: Compositionally controlled band gap and exciton dynamics [PMID: 26274456]. *The Journal of Physical Chemistry Letters*, 5(7), 1103–1109. <https://doi.org/10.1021/jz500280g>
- Kim, S., Márquez, J. A., Unold, T., & Walsh, A. (2020). Upper limit to the photovoltaic efficiency of imperfect crystals from first principles. *Energy Environ. Sci.*, 13, 1481–1491. <https://doi.org/10.1039/D0EE00291G>
- Kresse, G., & Furthmüller, J. (1996a). Efficiency of ab-initio total energy calculations for metals and semiconductors using a plane-wave basis set. *Computational Materials Science*, 6(1), 15–50. [https://doi.org/10.1016/0927-0256\(96\)00008-0](https://doi.org/10.1016/0927-0256(96)00008-0)
- Kresse, G., & Furthmüller, J. (1996b). Efficient iterative schemes for ab initio total-energy calculations using a plane-wave basis set. *Phys. Rev. B*, 54, 11169–11186. <https://doi.org/10.1103/PhysRevB.54.11169>
- Kresse, G., & Hafner, J. (1993). Ab initio molecular dynamics for liquid metals. *Phys. Rev. B*, 47, 558–561. <https://doi.org/10.1103/PhysRevB.47.558>
- Kresse, G., & Hafner, J. (1994). Norm-conserving and ultrasoft pseudopotentials for first-row and transition elements. *Journal of Physics: Condensed Matter*, 6(40), 8245–8257. <https://doi.org/10.1088/0953-8984/6/40/015>

Kresse, G., & Joubert, D. (1999). From ultrasoft pseudopotentials to the projector augmented-wave method. *Phys. Rev. B*, 59, 1758–1775. <https://doi.org/10.1103/PhysRevB.59.1758>

Lee, B. D., Park, W. B., Lee, J.-W., Kim, M., Pyo, M., & Sohn, K.-S. (2021). Discovery of lead-free hybrid organic/inorganic perovskites using metaheuristic-driven dft calculations. *Chemistry of Materials*, 33(2), 782–798. <https://doi.org/10.1021/acs.chemmater.0c04499>

Lundberg, S., & Lee, S.-I. (2017). A unified approach to interpreting model predictions. *CoRR*. <http://arxiv.org/abs/1705.07874v2>

Lux, T. C. H., Watson, L. T., Chang, T. H., Hong, Y., & Cameron, K. (2020). Interpolation of sparse high-dimensional data. *Numerical Algorithms*, 88(1), 281–313. <https://doi.org/10.1007/s11075-020-01040-2>

Manganaris, P., Desai, S., & Kanakkithodi, A. (2022). Mrs computational materials science tutorial. <https://doi.org/10.21981/D1J2-AR65>

Manganaris, P., Yang, J., & Mannodi Kanakkithodi, A. (2023). Multi-fidelity machine learning pervoskite composition vs band gap [In Preparation]. <https://doi.org/00.0000/000000000>

Mannodi-Kanakkithodi, A., & Chan, M. K. Y. (2022). Data-driven design of novel halide perovskite alloys. *Energy Environ. Sci.*, 15, 1930–1949. <https://doi.org/10.1039/D1EE02971A>

Mannodi-Kanakkithodi, A., & Chan, M. K. (2021). Computational data-driven materials discovery. *Trends in Chemistry*, 3(2), 79–82. <https://doi.org/10.1016/j.trechm.2020.12.007>

Mannodi-Kanakkithodi, A., Park, J.-S., Jeon, N., Cao, D. H., Gosztola, D. J., Martinson, A. B. F., & Chan, M. K. Y. (2019). Comprehensive computational study of partial lead substitution in methylammonium lead bromide. *Chemistry of Materials*, 31(10), 3599–3612. <https://doi.org/10.1021/acs.chemmater.8b04017>

Manser, J. S., Christians, J. A., & Kamat, P. V. (2016). Intriguing optoelectronic properties of metal halide perovskites. *Chemical Reviews*, 116(21), 12956–13008. <https://doi.org/10.1021/acs.chemrev.6b00136>

Mayo, D. G. (1996, April). *Error and the growth of experimental knowledge*. <https://doi.org/10.7208/9780226511993>

Mentel, L. (2014). mendeleeve – a python resource for properties of chemical elements, ions and isotopes. <https://github.com/lmmentel/mendeleeve>

Ouyang, R., Curtarolo, S., Ahmetcik, E., Scheffler, M., & Ghiringhelli, L. M. (2018). Sisso: A compressed-sensing method for identifying the best low-dimensional descriptor in an immensity of offered candidates. *Phys. Rev. Materials*, 2, 083802. <https://doi.org/10.1103/PhysRevMaterials.2.083802>

Park, H., Mall, R., Alharbi, F. H., Sanvito, S., Tabet, N., Bensmail, H., & El-Mellouhi, F. (2019). Exploring new approaches towards the formability of mixed-ion perovskites by dft and machine learning. *Physical Chemistry Chemical Physics*, 21(3), 1078–1088. <https://doi.org/10.1039/C8CP06528D>

Pedregosa, F., Varoquaux, G., Gramfort, A., Michel, V., Thirion, B., Grisel, O., Blondel, M., Prettenhofer, P., Weiss, R., Dubourg, V., Vanderplas, J., Passos, A., Cournapeau, D., Brucher, M., Perrot, M., & Duchesnay, E. (2011). Scikit-learn: Machine learning in python. *Journal of Machine Learning Research*, 12, 2825–2830.

Perdew, J. P., Burke, K., & Ernzerhof, M. (1996). Generalized gradient approximation made simple. *Phys. Rev. Lett.*, 77, 3865–3868. <https://doi.org/10.1103/PhysRevLett.77.3865>

Pilania, G., Mannodi-Kanakkithodi, A., Uberuaga, B. P., Ramprasad, R., Gubernatis, J. E., & Lookman, T. (2016). Machine learning bandgaps of double perovskites. *Scientific Reports*, 6(1). <https://doi.org/10.1038/srep19375>

Pu, W., Xiao, W., Wang, J.-W., Li, X.-W., & Wang, L. (2021). Screening of perovskite materials for solar cell applications by first-principles calculations. *Materials & Design*, 198, 109387. <https://doi.org/10.1016/j.matdes.2020.109387>

Ray, P., Reddy, S. S., & Banerjee, T. (2021). Various dimension reduction techniques for high dimensional data analysis: A review. *Artificial Intelligence Review*, 54(5), 3473–3515. <https://doi.org/10.1007/s10462-020-09928-0>

Shockley, W., & Queisser, H. J. (1961). Detailed balance limit of efficiency of pn junction solar cells. *Journal of Applied Physics*, 32(3), 510–519. <https://doi.org/10.1063/1.1736034>

Stanley, J. C., Mayr, F., & Gagliardi, A. (2020). Machine learning stability and bandgaps of lead-free perovskites for photovoltaics. *Advanced Theory and Simulations*, 3(1), 1900178. <https://doi.org/10.1002/adts.201900178>

- Steiner, S., Khmelevskiy, S., Marsmann, M., & Kresse, G. (2016). Calculation of the magnetic anisotropy with projected-augmented-wave methodology and the case study of disordered $\text{Fe}_{1-x}\text{Co}_x$ alloys. *Phys. Rev. B*, *93*, 224425. <https://doi.org/10.1103/PhysRevB.93.224425>
- Swanson, D. E., Sites, J. R., & Sampath, W. S. (2017). Co-sublimation of CdSeTe_{1-x} layers for CdTe solar cells. *Solar Energy Materials and Solar Cells*, *159*, 389–394. <https://doi.org/10.1016/j.solmat.2016.09.025>
- Tibshirani, R. (1996). Regression shrinkage and selection via the lasso. *Journal of the Royal Statistical Society: Series B (Methodological)*, *58*(1), 267–288. <https://doi.org/10.1111/j.2517-6161.1996.tb02080.x>
- Williams, L. (2022). *Sl3me – a python3 implementation of the spectroscopic limited maximum efficiency (slme) analysis of solar absorbers* (Version 1.0.0). <https://github.com/ldwillia/SL3ME>
- Xie, T., & Grossman, J. C. (2018). Crystal graph convolutional neural networks for an accurate and interpretable prediction of material properties. *Physical Review Letters*, *120*(14). <https://doi.org/10.1103/physrevlett.120.145301>
- Yan, Y., Yin, W.-J., Shi, T., Meng, W., & Feng, C. (2016). Defect physics of $\text{CH}_3\text{NH}_3\text{PbX}_3$ ($x = \text{i, br, cl}$) perovskites. *Organic-Inorganic Halide Perovskite Photovoltaics*, 79–105. https://doi.org/10.1007/978-3-319-35114-8_4
- Yang, J., Manganaris, P. T., & Mannodi Kanakkithodi, A. K. (2023). A high-throughput computational dataset of halide perovskite alloys. *Digital Discovery*. <https://doi.org/10.1039/d3dd00015j>
- Yang, J., & Mannodi-Kanakkithodi, A. (2022). High-throughput computations and machine learning for halide perovskite discovery. *MRS Bulletin*, *47*(9), 940–948. <https://doi.org/10.1557/s43577-022-00414-2>
- Yang, L., & Shami, A. (2020). On hyperparameter optimization of machine learning algorithms: Theory and practice. *Neurocomputing*, *415*, 295–316. <https://doi.org/10.1016/j.neucom.2020.07.061>
- Yin, W.-J., Yang, J.-H., Kang, J., Yan, Y., & Wei, S.-H. (2015). Halide perovskite materials for solar cells: A theoretical review. *Journal of Materials Chemistry A*, *3*(17), 8926–8942. <https://doi.org/10.1039/c4ta05033a>

Yu, L., & Zunger, A. (2012). Identification of potential photovoltaic absorbers based on first-principles spectroscopic screening of materials. *Physical Review Letters*, 108(6). <https://doi.org/10.1103/physrevlett.108.068701>

Zhang, H., Nazeeruddin, M. K., & Choy, W. C. H. (2019). Perovskite photovoltaics: The significant role of ligands in film formation, passivation, and stability. *Advanced Materials*, 31(8), 1805702. <https://doi.org/10.1002/adma.201805702>

Zhu, S., Ye, J., Zhao, Y., & Qiu, Y. (2019). Structural, electronic, stability, and optical properties of cspb1-xsnxibr2 perovskites: A first-principles investigation. *The Journal of Physical Chemistry C*, 123(33), 20476–20487. <https://doi.org/10.1021/acs.jpcc.9b04841>

ADDITIONAL FIGURES

Learning Curves

Cross-validation within the training set is the only way of checking the generality of models during the grid search. Identifying the validation split size is necessary to obtain an understanding of how much data is needed to train a model that can generalize.

Learning curves are computed for each scorer. Notice that the error metrics are negated for consistency with the R^2 and ev scores; the greater the number, the better the model performs.

More data offers better chances. However, the smaller the split, the longer and more expensive the loop training becomes, e.g. 10-fold splits makes for 10 sample scores at each partition size. Meaning, 90% of the training set is used for actual training and the remaining 10% is used for validation and this is repeated 10 times.

Shuffling is performed prior to generating each fold. The shuffle is seeded with a deterministic random state to ensure scores are comparable across partition size

Feature Distributions

GPR SHAP analysis

SIS+RFR SHAP analysis

SIS+GPR SHAP analysis

Known Clustering in t-SNE Projections

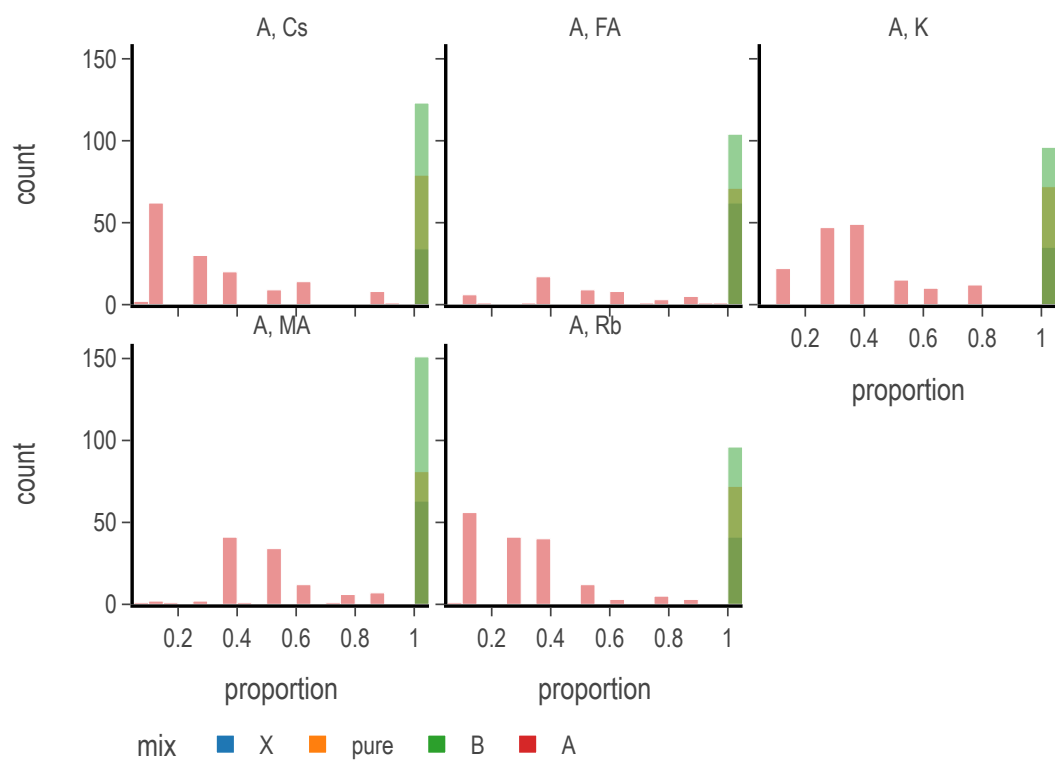


Figure 1. Normalized Distribution of A-site Constituents

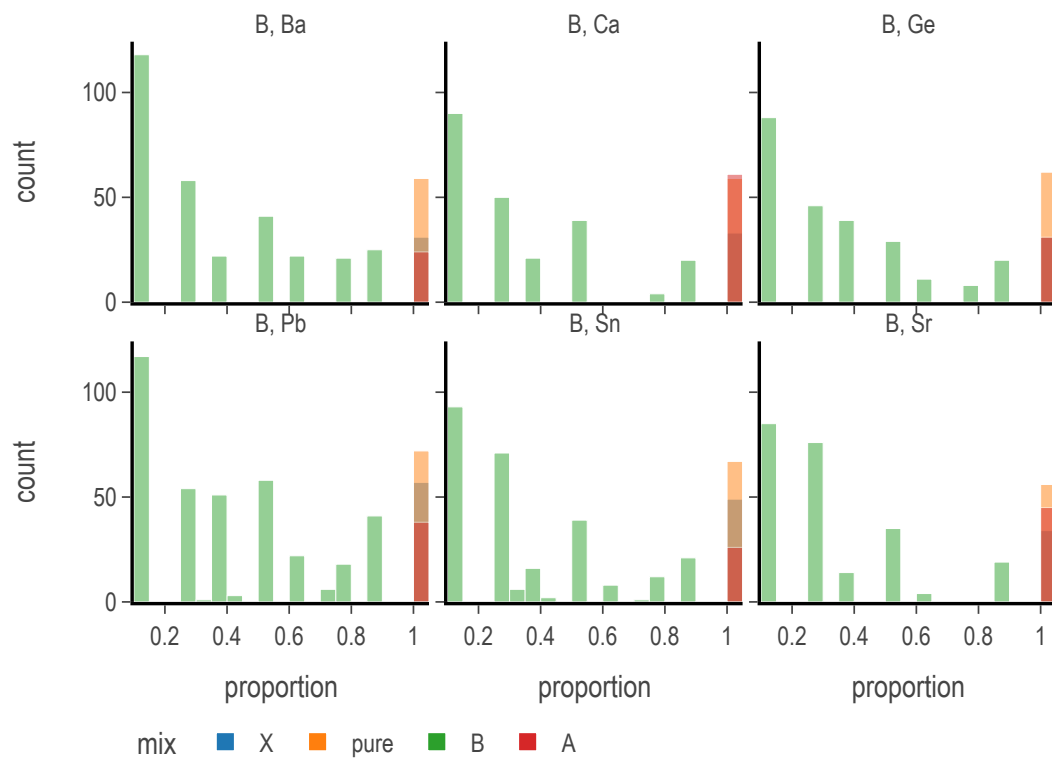


Figure 2. Normalized Distribution of B-site Constituents

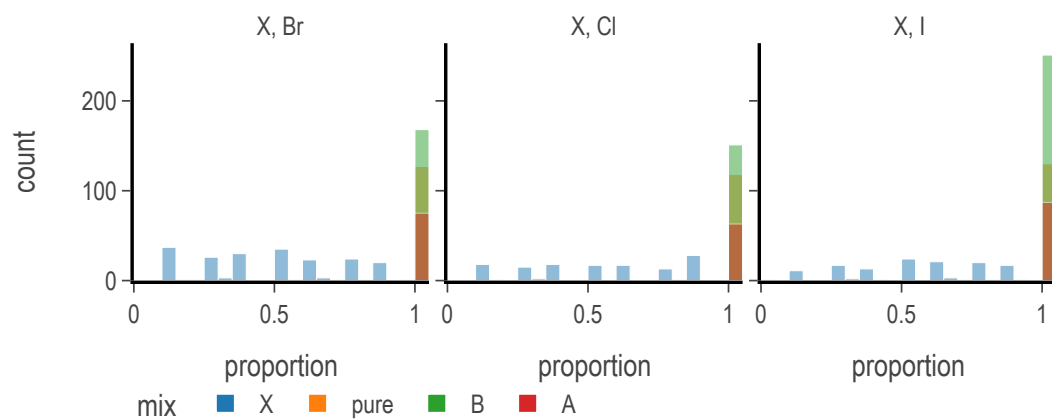


Figure 3. Normalized Distribution of X-site Constituents

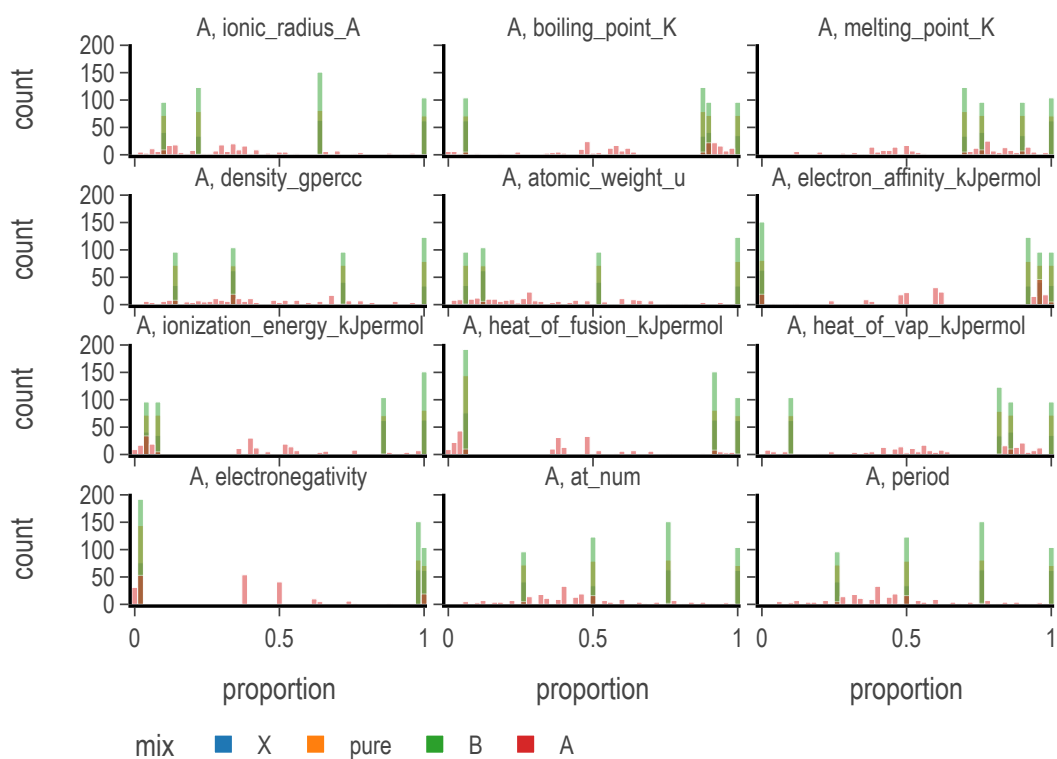


Figure 4. Distributions of Mean A-Site Properties

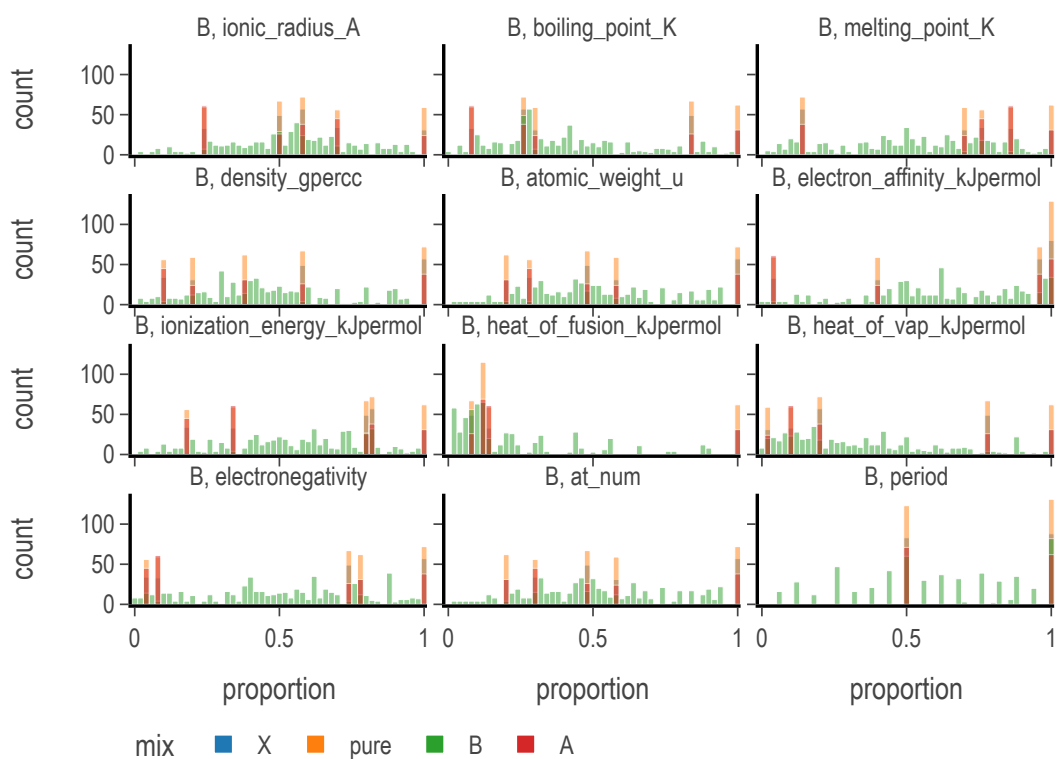


Figure 5. Distributions of Mean B-Site Properties

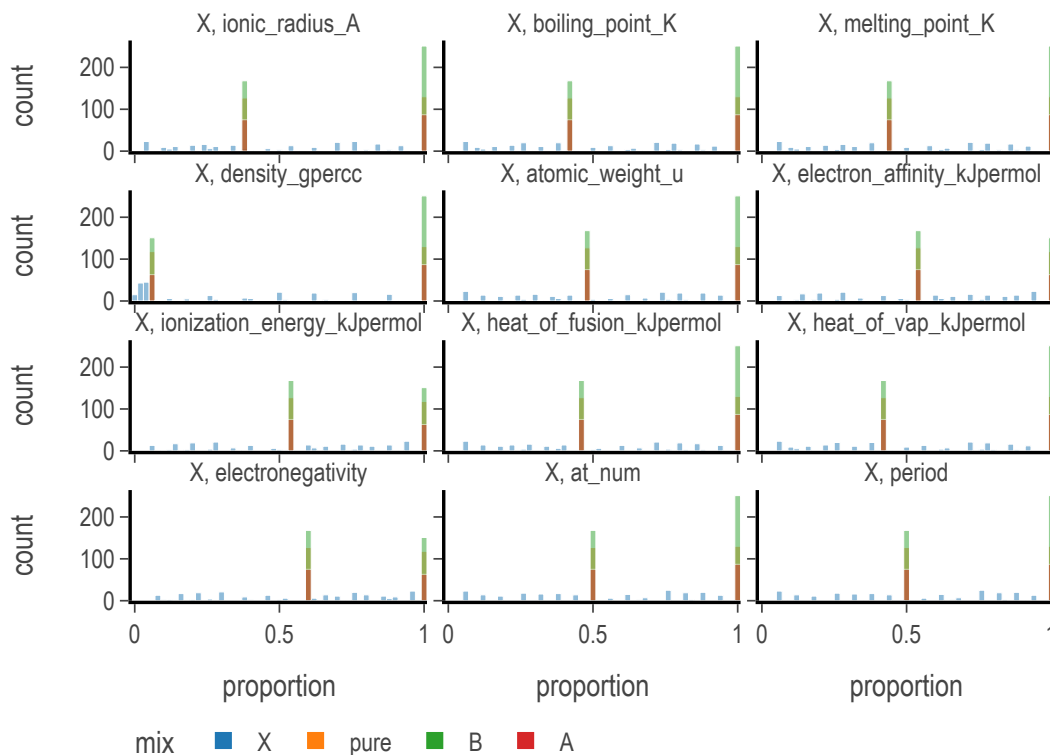


Figure 6. Distributions of Mean X-Site Properties

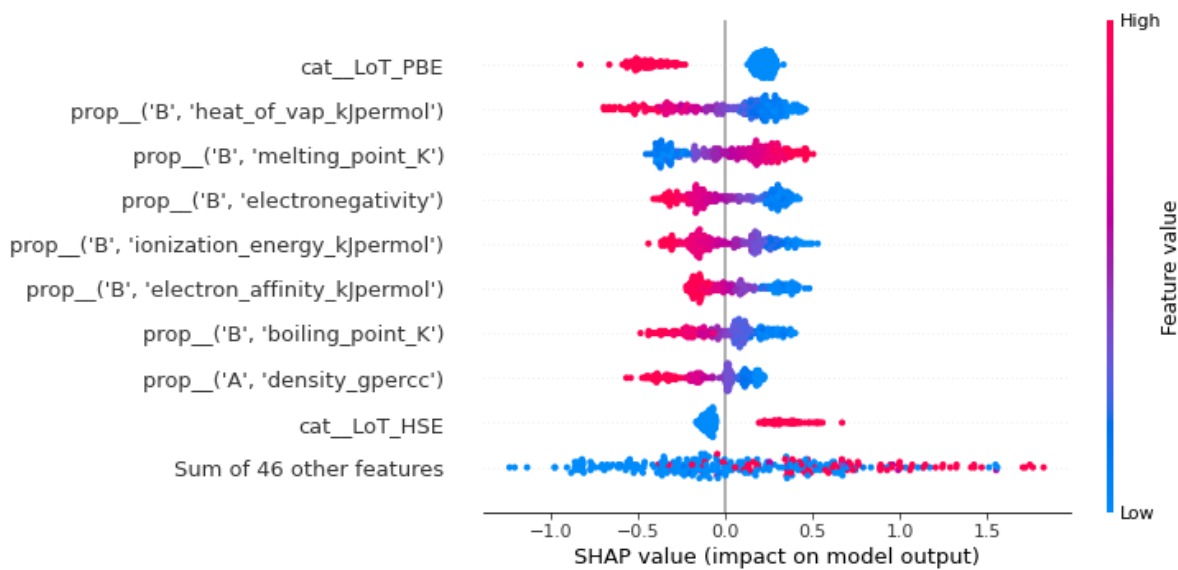


Figure 7. Gaussian Process Regression Band Gap SHAP Values

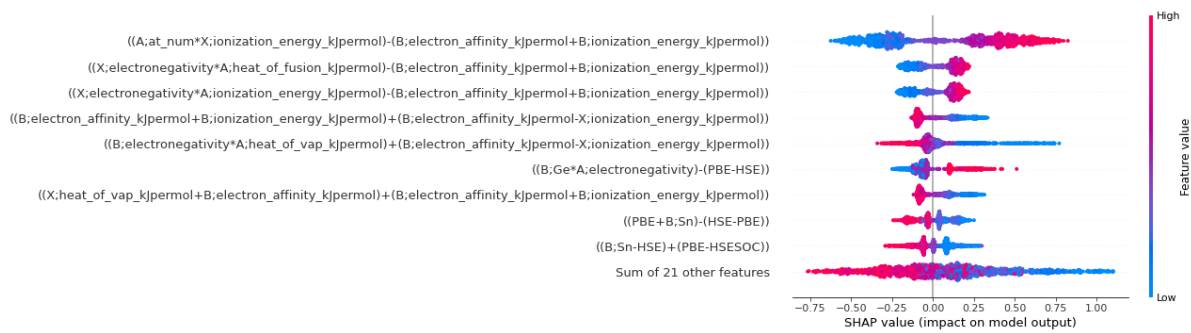


Figure 8. Random Forest Regression Band Gap on SIS domain SHAP Values

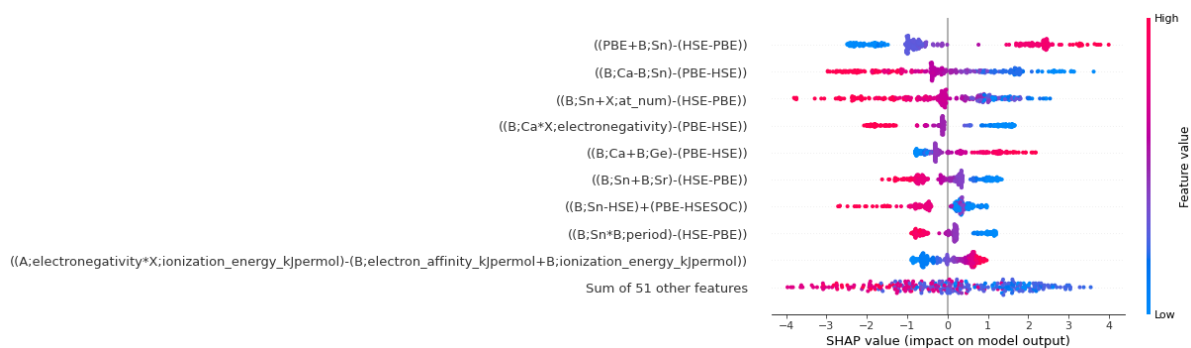


Figure 9. Gaussian Process Regression Band Gap on SIS domain SHAP Values

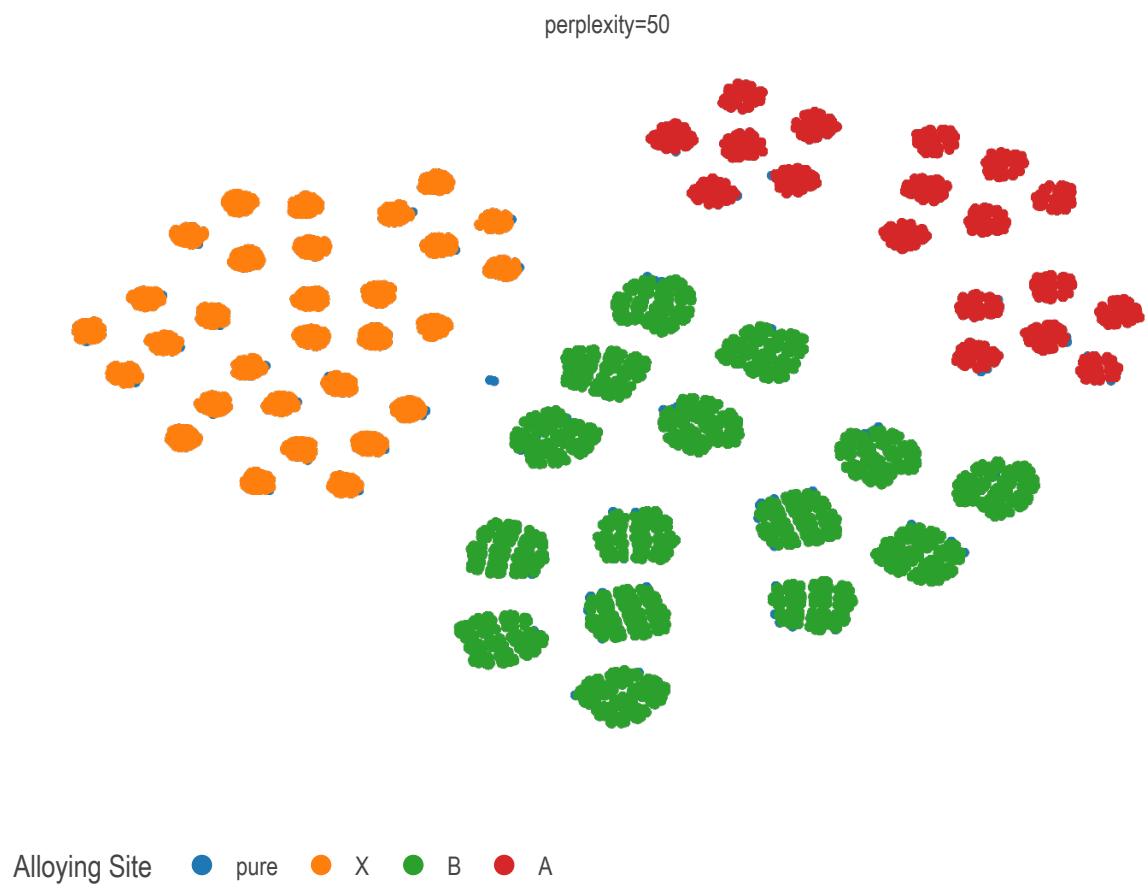


Figure 10. Projection of sample space via t-SNE overlaid with labels indicating site of mixing

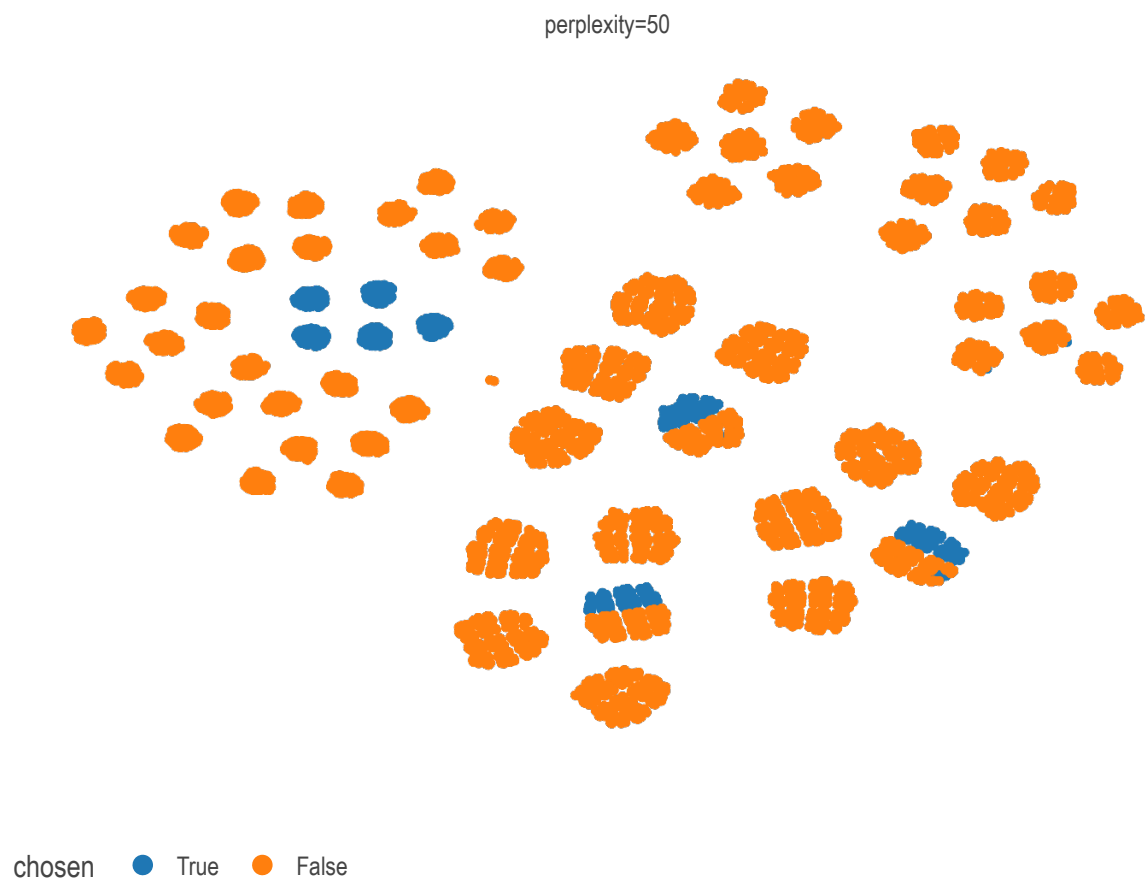


Figure 11. Projection of sample space via t-SNE overlaid with labels indicating presense of data points in screened subset